ALIGNMENT OF A STED MICROSCOPE USING FCS

CHARACTERIZATION AND ALIGNMENT OF THE STED DOUGHNUT USING FLUORESCENCE CORRELATION SPECTROSCOPY

By CHARMAINE TRESSLER, M. Sc.

A Thesis Submitted to the School of Graduate Studies in Partial Fulfilment of the Requirements for the Degree Master of Science

McMaster University MASTER OF SCIENCE (2013) Hamilton, Ontario(Physics)

TITLE: Characterization and alignment of the STED doughnut using Fluorescence Correlation Spectroscopy

AUTHOR: Charmaine Tressler, M.Sc. (McMaster University)

SUPERVISOR: Professor C. Fradin

NUMBER OF PAGES: viii, 77

ABSTRACT

This report primarily focuses on effectively obtaining a Stimulated Emission Depletion fluorescence (STED) microscope, while using Fluorescence Correlation Spectroscopy (FCS) as a guide for the alignment of the system. STED is a super-resolution microscopy technique that has gained favour in the biological sciences due to its ability to successfully resolve sub-diffraction structures within live cells. Moreover the ease with which it can be combined with FCS has extended the applications of this technique to the study of the dynamics within a system as well. The central premise of this work focuses around building a STED-FCS system and developing an alignment tool for obtaining a symmetric STED doughnut. Since the point spread functions (PSF) seen in confocal microscopy can be generally approximated by a Gaussian function, we approximate the doughnut PSF with a difference of Gaussian functions. We calculated an autocorrelation function (ACF) corresponding to the simplified Gaussian form of the doughnut PSF and we found that this ACF contained three very similar diffusion times, all inversely proportional to the dye diffusion coefficient. In agreement with the fact that the doughnut PSF is spread out compared to the purely Gaussian PSF, the doughnut ACF amplitude is lower and its average diffusion time large. Lastly we calculated the quality factor, which is the product of the amplitude of the correlation function with the average intensity, Q=G(0)*I, for the purposes of alignment of the system. When translating the confocal pinhole along an axis of the doughnut we were able to identify the centre of the doughnut due to the presence of a minimum in Q which can be very handy for alignment of the doughnut with respect to the pinhole. This operation is essential when aligning the excitation and STED beam. For future work, a road map for alignment of the two beams in the focal plane is also presented utilizing the cross correlation function between the two beams.

ACKNOWLEDGEMENTS

I would like to thank Dr. Cecile Fradin for all the help and support she gave for the completion of this thesis, for guiding me at every step and ensuring that I stay on track. I would also like to thank my committee members; Dr. K. Dalnoki-Veress and Dr. J. Preston for their valuable input in my project.

I would like to thank all the members of the Fradin Lab for assisting me in my project whenever I needed help, especially Amit Patel for helping me align my set-up on various occasions and for writing the analysis program.

TABLE OF CONTENTS

LIST OF FIGURES

LIST OF ABBREVIATIONS

ACF - Autocorrelation Function

APD - Avalanche Photo Diode

BP-FPALM- Biplane Fluorescence Photo-activable Localization Microscopy

CPP - Count per Particle

CW - Continuous Wave

ER - Endoplasmic Reticulum

FCS - Fluorescence Correlation Spectroscopy

FPALM - Fluorescence Photo-activable Localization Microscopy

FWHM - Full-Width-at-Half-Maximum

GSD - Ground State Depletion

PBS - Phosphate Buffered Saline

PMT - Photo Multiplier Tube

PSF - Point Spread Function

STED - Stimulated Emission Depletion Microscopy

STORM - Stochastic optical reconstruction microscopy

tRNA - transfer Ribonucleic Acid

VLS-FCS - Variable Length Scale Fluorescence Correlation Spectroscopy

CHAPTER 1

Introduction

1.1 Scaling in biology

The unaided human eye is incapable of observing objects smaller than about 0.1 mm in diameter. Since cells and bio-molecules fall significantly below this length scale the invention of the light microscope in the early 1600's was a mandatory step in the advancement of biological and medical research. With further improvements in technology, imaging of cells and the structures within them has become routine and efforts are being made to improve the resolution of the optical microscope even further to understand intricate details involved in the functioning of the cell. To put biological scales into perspective, a skin cell is about 30 μm in diameter, the bacterium *Escherichia coli* is about 2 μm in length, the influenza virus is about 130 nm and a tRNA molecule is about 7 nm. Most of these objects are not resolvable using a light microscope and techniques such as electron microscopy which can image objects down to the Angstrom scale are ineffective in studying live samples due to the need for chemical fixation. Other techniques such as near field optical microscopy are either invasive or destructive to the system. Therefore in order to study sub-cellular structures and molecules within live cells it would be extremely useful to devise optical methods that are able to image at this length scale.

1.2. Diffraction limit

Under the umbrella of optical microscopy, far-field fluorescence microscopy has gained considerable popularity over the past few decades because of its ability to specifically image the desired biomolecules non-invasively in cells and tissues. The only drawback to this technique is its inability to resolve any structures that are smaller than ~250 nm in the focal plane. This limitation known as the Abbe Limit arises due to the wave nature of light which results in diffraction of light wavefronts as they pass through the circular back aperture of the objective lens. With such a microscope, the image of a point object is in the shape of an Airy disk whose full-width-at-half-maximum (FWHM) is defined by the relationship (Cole et. al, 2011):

$$d = \frac{0.51\lambda}{(n * Sin\ \theta)} \qquad [1.1]$$

Here λ is the wavelength of light used, n is the index of refraction of the medium and θ is the half angle over which the objective gathers light from the sample. It is clear from this definition that the size of the focal spot is dictated by the wavelength of light used and as long as one remains in the visible region it cannot be lower than 250 nm. In order to break this barrier one can image with lower wavelength light sources such as ultraviolet and X-rays but this comes with risk of damaging live cells. The resolution also depends on the numerical aperture of the objective lens which is defined as:

$$NA = n * Sin\ \theta \qquad [1.2]$$

Manufacturers of objective lenses tend to focus on designs for their objectives which give them a higher numerical aperture, which is done effectively by increasing the angle θ or the index of refraction, hence the use of oil immersion lenses. The index of refraction for air is approximately 1, for water it is 1.33 and for typical immersion oils it is 1.51. Based on equation 1.1 having an oil immersion objective lens would decrease the size of the focal spot and result in better image resolution. A fluorescence technique that has gained recognition for exploiting this idea is 4pi microscopy (Hell and Stelzer, 1992), which is able to resolve in the axial plane and give resolutions in the 100-140 nm range, which is about a five-fold improvement. This is done through the use of a set of opposing objective lenses with high numerical aperture focused onto the same spot. Normally the axial resolution with the highest aperture objective is $\sim 2\lambda/n$, but with 4pi microscopy it can be reduced to $\lambda/4n$. This is so because when two focused counter propagating wave-fronts are coherently superimposed it increases the overall aperture of the system, thus sharpening the point spread function (PSF) in the optical axis (Gugel et al., 2004). Objective lens designs have their own limitations since $\sin\theta < 1$ and with $n \sim 1.6$ at best, the numerical aperture has to be less than or equal to 1.5. With optimal conditions, this results in a minimum focal size of about 1/3 of the wavelength of the light used. However, recently other ground breaking techniques collectively known as super-resolution techniques have been explored that are able to break the diffraction barrier and have many applications in the life sciences.

1.3 Super resolution microscopy

The idea behind super-resolution imaging is to be able to resolve two or more nano-scaled objects that are less than $\lambda/2n$ away from each other ($\sin\theta \approx 1$, from equation 1). Super resolution microscopy comprises of an array of techniques that can be loosely classified as either being targeted or stochastic. In the targeted read-out mode the bright state of a fluorophore is contracted to a sub-diffraction sized spot by driving the rest of the peripheral area to a dark state. Whereas, in the stochastic read out mode the fluorophore is required to be switchable between a dark and bright state. Fluorophores from random positions which are more than $\lambda/2n$ apart from each other are activated to the bright state and their coordinates are sequentially calculated from the diffraction spot with great precision. Some techniques that implement the targeted read out mode are Stimulated Emission Depletion Microscopy (STED) (Hell and Wichmann, 1994), Ground State Depletion Microscopy (GSD) (Hell, S. and Kroug, M., 1995) and Structured Illumination Microscopy (SIM) (Gustafsson, 2000). Techniques that stochastically read out their fluorophores are Photoactivated Localization Microscopy (PALM) (Betzig et al., 2006) and Stochastic optical reconstruction microscopy (STORM) (Rust et al., 2006). The advantages of the targeted read out mode and specifically STED are its ability to image live samples with resolutions down to 40 nm (Hein et. al., 2008), the ease with which it can be combined with 4pi and other such techniques to get three dimensional images as well as the ability to study dynamics within a system by combining it with Fluorescence Correlation Spectroscopy (FCS). The only inconvenience associated with STED is the requirement for an advanced optical set-up and precise beam alignment.

1.3.1 Stochastic super-resolution methods

Photoactivable or photoswitchable fluorophores are widely available now and their properties have been exploited to give rise to techniques such as PALM, STORM and variations of these techniques. In STORM/PALM, the photoactivable fluorophores are initially found in a dark state and then irradiated with light which causes them to fluoresce. The fluorescence signal of a single emitter, which is diffraction limited, is read out and the position is determined by approximating the point spread function (PSF) with a Gaussian function. This emitter is then switched off and neighbouring fluorophores are activated. This process is repeated many times till an image can be formed. The only caveat is that less than one activated fluorophore should be present within a diffraction limited spot. The precision mainly depends on the number of photons emitted and can reach nanometer accuracy. In 2007, Bates et. al demonstrated multicolour super-resolution imaging of DNA and mammalian cells with 20-30 nm resolution using STORM (Bates, 2007). 3-D imaging of cells has also been accomplished using BP-FPALM (biplane fluorescence PALM) which combined basically a double plane detection scheme with PALM and delivered resolutions of 30x30x75 nm (Juette et. al., 2008). Now, the challenge for all methods employing this stochastic read out method is that they are not compatible with live cell imaging because normally several thousand images have to be recorded and combined which drastically reduces the temporal resolution.

1.3.2 Confocal microscopy and STED

STED microscopy was introduced by Stefan Hell in 1994 (Hell and Wichmann, 1994) and can be roughly considered to be an extension of confocal microscopy. In confocal microscopy the excitation laser beam is focused onto a sample and the desired area is scanned either using scanning mirrors or a piezo stage. The fluorescence emission passes through a pinhole, to get rid of out of focus signal, and is finally detected using photomultiplier tubes (PMT) or avalanche photodiodes (APD). The only and most important difference in STED microscopy is the need for a second laser beam informally known as the STED beam. The role of the STED beam is to inhibit fluorescence using stimulated emission.

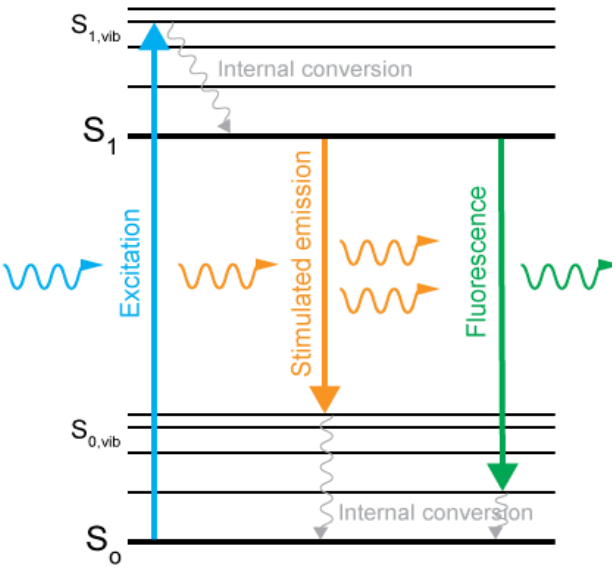

Figure 1 - Jablonski diagram showing the electronic states of a fluorophore.

Spontaneous emission (fluorescence) occurs through excitation of the fluorophore and a redshifted photon is released. Stimulated emission occurs when a STED photon (even more redshifted) stimulates the release of an identical photon, hence inhibiting fluorescence.

(Max Plank Institute for Biophysical Chemistry, 2012)

In the Jablonski diagram in Figure 1, we see that a fluorophore gets excited by absorbing a suitable photon and is sent to a higher energy level (from S_0 to S_{1vib}). It then drops down

to a lower sublevel within the excited levels and the energy is dissipated (from S_{1vib} to S_1). This occurs generally because of molecular collisions and the relaxation time for this is about 1-5 picoseconds (Hell and Wichmann , 1994). Following this, spontaneous emission occurs where the electron falls back to a ground state sublevel higher than S_0 and hence a photon with a longer wavelength is emitted. The average fluorescence lifetime is typically about 2 ns (Hell and Wichmann, 1994). For stimulated emission to occur, a red-shifted photon, called the STED photon is introduced which stimulates the electron to drop down to S_{0vib} from S_1 before spontaneous emission can occur. After the electron falls back to the ground state, the STED photon is released along with an identical photon emitted as a result of the drop, while no fluorescence photons are emitted. The STED photons are filtered out of the system using emission filters and hence are never detected.

The main concept behind STED microscopy is to have the STED beam focused and superimposed on the excitation beam such that it can deplete fluorescence only from the periphery of the diffraction limited excitation spot and leave a sub-diffraction sized excitation spot in the centre. This is accomplished through the use of a vortex phase plate which changes the shape of the laser beam into a torus or doughnut upon focusing, with the centre of the doughnut having a zero intensity point (Figure 2). A vortex phase plate as the name suggests creates an optical vortex. This is done by inducing a phase shift of 2π onto an oncoming wavefront by employing a helical phase ramp (Moneron et. al., 2010). Fundamentally, if light is twisted around its axis of travel like a corkscrew, there is destructive interference at the centre and an optical singularity is created.

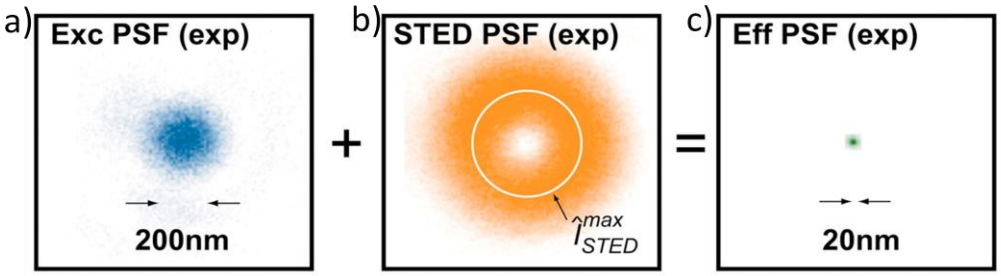

Figure 2 - Experimental (exp) point spread functions (PSF) of the excitation (a), STED (b) and resultant fluorescence spot (c).
Upon superposition the STED spot quenches fluorescence from the periphery of the diffraction limited excitation spot (~200 nm) through stimulated emission depletion. The resulting sub-diffraction fluorescence spot is about 20 nm in width. (Donnert, G. et. al,

It is important to mention here that the STED doughnut created upon focusing with an objective lens is also diffraction limited. Typical STED and excitation intensity profiles are shown in figure 3. The diffraction limited excitation spot is approximated with a Gaussian function here. One can see that upon overlaying the two profiles, the intensity plays a crucial role in determining the width of the resulting excitation spot in the centre. By increasing the intensity of the STED beam, the resultant FWHM of the Gaussian is getting narrower as can be seen in Figure 3. Hence if the intensity of the STED beam is high enough one can obtain excitation spots that are just a few nm in size.

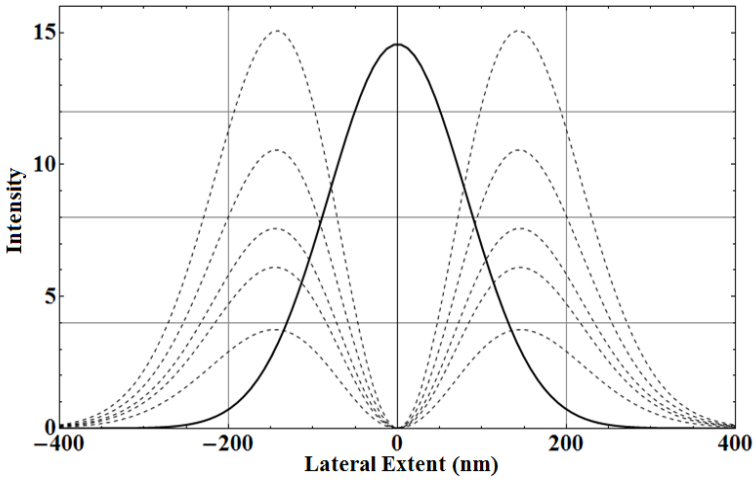

Figure 3 - Calculated doughnut (dotted) and Gaussian (solid) intensity profiles.

An increase in STED intensity results in a smaller fluorescence spot. These profiles were created on Mathematica by approximating the doughnut as a difference of two Gaussian functions.

The formula that governs the relationship between spot width and intensity is (Wildanger et. al., 2009):

$$d_{STED} = \frac{\lambda}{2NA\sqrt{1+\frac{I}{I_s}}} \quad [1.3]$$

Here I is the intensity at the maximum of the STED doughnut and I_s is the saturation intensity which is a characteristic of the dye.

In the literature there are several examples of super resolution images obtained using STED microscopy with various fluorescent dyes (Appendix D). Initially STED was realized with pulsed laser sources but recently continuous wave (CW) lasers have become quite popular due to their low costs and simplicity (Willig et. al., 2007). Pulsed lasers require the STED pulses to be prepared and stretched to generally in the picosecond range so they are smaller than the fluorescence lifetime of about 2ns. The two lasers also need to be synchronized in order to obtain proper quenching. In order to avoid this a few groups have experimented with continuous wave lasers over the past few years with great success. In 2007, Willig et.al., reported a STED experiment with 635 nm excitation and 760 nm STED and imaged neurofilaments in human neuroblastoma labeled with the dye Atto 647 and obtained a lateral resolution of about 29 nm. In 2010, Moneron et. al performed STED microscopy on live PtK2 cells whose Endoplasmic Reticulum (ER) were labeled with the fluorescent protein Citrine and achieved resolutions less than 65 nm.

A technique that has worked well with STED to obtain 3-dimensional super-resolution is 4pi microscopy. By itself 4pi is not sufficient to provide a good isotropic

resolution since it only targets the axial plane. It does not however have the limitations of the stochastic read-out methods mentioned earlier and when combined with two photon excitation has been used for 3-dimensional imaging of fixed and live cells with ~80 nm resolution.(Gugel et. al., 2004). This implies that it can also be easily implemented in a STED set-up and has been done successfully in the past with an image resolution of ~50 nm (xyz) (Dyba et. al , 2003). Another way to obtain a 3-dimensional STED microscope is with the addition of another STED beam as was demonstrated by Wildanger et. al., in 2009. STED has so far demonstrated exceptional results of super-resolution microscopy in living cells with good time resolution. The simplicity with which STED can be combined with single molecular dynamics techniques such as FCS was a major attraction for us, and one of the chief reasons for building a STED-FCS instrument. The following two sections expand on FCS as an excellent analytical tool to study molecular dynamics, specifically diffusion, within cells.

1.4 Diffusion and FCS

Diffusion is widely studied in both the interior and exterior of membrane systems within cells and results from the thermal, random movement of molecules. Since diffusion is one of the key processes through which most transport occurs within a cell it is important to devise methods that can study it at the molecular level. In some cases diffusion can be categorized as either being simple or anomalous if it can be represented by the following relationships. Simple diffusion occurs in isotropic fluids where the mean square displacement of a particle scales linearly with time. The solution of the diffusion equation gives:

$$\langle r^2(t)\rangle \sim Dt \qquad [1.4]$$

This relationship breaks down when the medium for diffusion is a more complex media and one then sees the mean square displacement obeying a power law:

$$\langle r^2(t)\rangle \sim \Gamma \times t^{\alpha} \sim (\Gamma t^{\alpha-1})t \qquad [1.5]$$

The diffusion coefficient $D(t)=\Gamma t^{\alpha-1}$ with Γ being a constant, now depends on the timescale of the measurement. If the measured α is not equal to 1, the diffusion is considered anomalous. For this reason α is known as the anomalous exponent (Banks, S. and Fradin, C., 2005).

1.4.1 Fluorescence Correlation Spectroscopy

FCS is a key correlation analysis tool that has been used extensively to study molecular dynamics within biological systems through which, parameters such as diffusion coefficients, concentration of fluorescent particles and kinetic chemical reaction rates are extractable (Ries, J. and Schwelle, P., 2008). It relies on the analysis of the fluctuations of the fluorescence intensity collected from a very small observation volume (generally the size of the focal spot ~250 nm width, ~500 nm height) and requires a low concentration of fluorophores. The intensity fluctuates due to Brownian diffusion of the particles and the diffusion time, which is the average time it takes for the particle to travel across the observation volume (τ_D), as well as the width of the observation volume (ω_0) can be used to calculate the diffusion coefficient according to:

$$D = \frac{{\omega_0}^2}{4\tau_D} \qquad [1.6]$$

τ_D is measurable using this technique and ω can be first calculated using a dye of known diffusion coefficient.

It may be apparent at this time that FCS seems best suited to be implemented in a confocal type set-up since the observation volume is just the Gaussian excitation spot of the laser beam. The only extra accessory that is required is a correlator that performs the analysis of the signal and outputs a correlation function. A correlation function measures the self-similarity of a signal over a time, τ, commonly known as the lag time. At lag times smaller than a characteristic timescale the processes are correlated and at lag times larger than the characteristic time scale, processes are not correlated. In the case of diffusion, this characteristic timescale is the diffusion time. A typical correlation function with a Gaussian illumination profile is shown in figure 4.

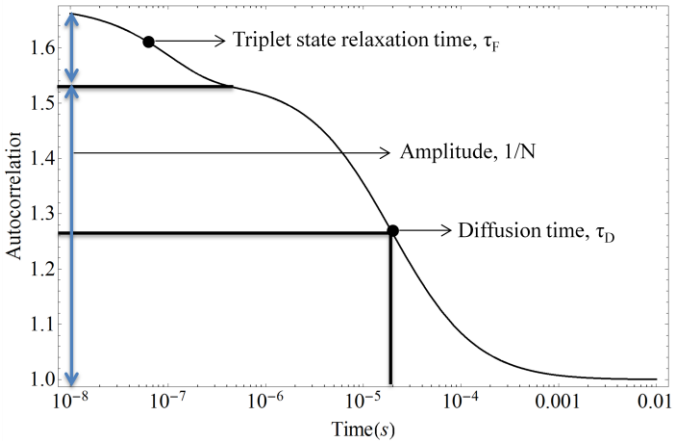

Figure 4 - Autocorrelation as a function of time (s).
The figure shows the average diffusion time, which is the amount of time it takes for a fluorophore to travel across the focal volume. Also shown is the triplet state relaxation time and the amplitude of the correlation function, which is the inverse of the number of fluorophores present in the focal volume.

Some discernible features are the diffusion time, number of particles and triplet state relaxation time (shown on the graph). The derivation of the function that can be used to fit this curve assuming fluorescence fluctuations are due to diffusion and triplet state photophysics is shown in Appendix A. The resultant model correlation function for a 3-D Gaussian illumination profile including the triplet state term (Widengren et al., 1994) is:

$$G(\tau) = \frac{1/N}{\left(1+\left(\frac{\tau}{\tau_D}\right)^{\alpha}\right)\left(1+\frac{1}{S^2}\left(\frac{\tau}{\tau_D}\right)^{\alpha}\right)^{1/2}}\left(1 + \frac{T}{1-T}e^{-\frac{\tau}{\tau_T}}\right) \quad [1.7]$$

The constant, α, is the anomalous exponent which is equal to 1 for simple diffusion. Solving for G(0) when T=0, gives 1/N where N is equal to the average number of fluorescing molecules present in the detection volume and can be estimated from the amplitude of the correlation function. The constant $S = \omega_Z/\omega_0$ ~5 represents the aspect ratio of the detection volume and it influences the sharpness of the autocorrelation function decay. T is the fraction of molecules in the triplet state and τ_T is the triplet state relaxation time.

For a fluorophore of known diffusion coefficient and brightness, the diffusion time and number of particles can be an indicator of the size of the detection volume (equation 1.6). Since it is expected that in a STED microscope the detection volume would be smaller, these parameters can be used to assess the success of a STED alignment, which inspired this work. Another important indicator of the quality and alignment of the laser beam, and of the correct position of the pinhole is the average count per particle (CPP). This quantity reports the number of photons detected per second per fluorophore and can be calculated by multiplying 1/N by the average intensity over the measured time, CPP=I/N. The work by Koppel, D. in 1974 shows that the critical parameter governing the statistical accuracy of the FCS experiment is the count per particle. Photon noise, which arises due to the random nature of photon emission is indicated by a drop in CPP especially at low lag times. Since an increase in CPP corresponds to a decrease in photon noise quadratically, it can be used as a guide to maximize the detection efficiency of the FCS set-up. In

addition, if the excitation is not symmetric then the CPP drops which is reflected through a decrease in the height of the correlation curve as well as a decrease in intensity. This implies that the CPP can be an indicator of the quality of the alignment and one should strive to always maximize it in order to achieve a correlation function with the highest signal-noise ratio that would represent the dynamics of the system accurately.

STED-FCS fits the requirements needed for single molecular studies perfectly. In order to study single molecules the concentration of fluorescent molecules needs to be low, in the nM range, which can be accomplished in vitro with confocal microscopy. Unfortunately, the concentration of molecules in biological conditions are often far above the nM range and a possible solution would be to reduce the size of the window through which these molecules are being viewed (Kastrup et. al, 2005). A larger confocal spot usually averages over the nanoscale dynamics but a smaller STED spot would effectively probe details of molecular dynamics whose disclosure is impossible with conventional confocal microscopy. A great example of the resolving power of STED-FCS is the work by Eggeling et. al, published in 2009. By studying living mammalian cells using FCS and comparing results between confocal and STED experiments they were able to show the existence of lipid nanodomains, or rafts, which are formed with the assistance of cholesterol and are responsible for impeding their diffusion in the plasma membrane. With a focal detection area of 30 nm and accompanying decrease in diffusion time they were able to show a hindered lipid diffusion which was caused by a brief trapping of the molecules in a cholesterol mediated complex smaller than 20 nm in diameter. While the confocal curves could be explained by normal diffusion with just a slower transit time,

the STED curves showed anomalous diffusion and hence revealed this trapping behaviour. Our reasons for studying STED-FCS are quite analogous to this study and will be discussed in more detail next.

1.4.2 Variable length-scale FCS (VLS-FCS) and its use for anomalous diffusion diagnosis

Variable length-scale FCS is a variation of FCS that probes diffusion over different length scales by increasing the confocal observation volume. Previous experiments on VLS-FCS were done by Daniel Banks (Banks, D., 2008) using 40 nm fluorescent beads either in solution (PBS) or crowded media, mimicked by agarose gel at different concentrations. The reason for studying crowded media is that within cells the different constituents are present at high concentrations and make the medium crowded causing anomalous diffusion of proteins and nucleic acid (Weiss, M. et al., 2004) . Since it is known that the diffusion coefficient is length scale dependent when the diffusion is anomalous, it justifies studying the system at different length scales in order to truly diagnose anomalous behaviour.

In the VLS-FCS experiments, the width of the beam illuminating the back aperture of the objective lens was incrementally reduced with an iris which resulted in larger observation volumes. Combining this with accompanying pinholes that optimized the background rejection produced observation volumes with radii ranging from approximately 0.4 μm to 2 μm. The correlation functions obtained from this experiment for beads in 1.2% agarose gel were analyzed by rescaling the horizontal axis. This was done by dividing the time by

the diffusion time obtained from the fits of the correlation curve for each observation volume. By normalizing in this manner the difference in shape between the correlation curves becomes more apparent as can be seen in Figure 5. There is a clear distinction between the different length scales especially at longer correlation times even though it is evident at the shorter times. A sharper s-curve represents normal diffusion whereas a flatter curve represents anomalous behaviour. Since the beads have been suspended in 1.2% agarose gel it is enough to mimic crowdedness and render the diffusion anomalous but one can see that this behaviour becomes more apparent only at the smaller length scales (black curve, 0.411 μm). Figure 6 compares the anomalous coefficient, α, acquired from the fits of the correlation data from beads in PBS and beads in 1.2% agarose gel at a wide range of length scales.

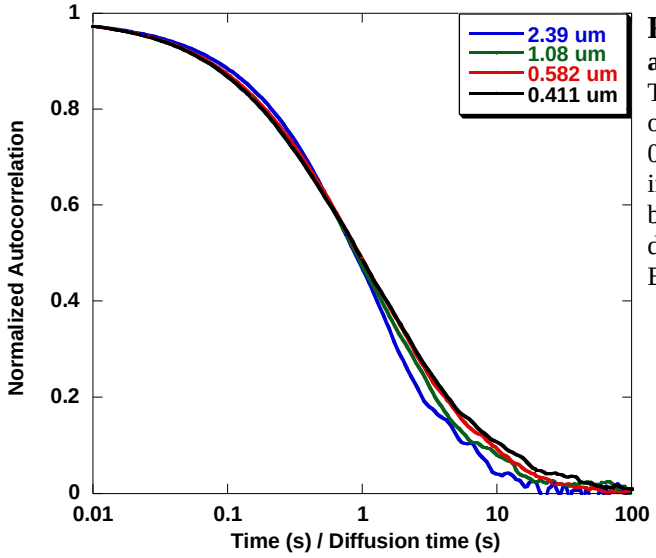

Figure 5: Normalized autocorrelation as a function of rescaled time.
The four curves correspond to decreasing observation volumes from 2.39 μm to 0.411 μm. The shape of the curves indicate a trend towards anomalous behaviour as the observation volume decreases.
Banks, D., (2008)

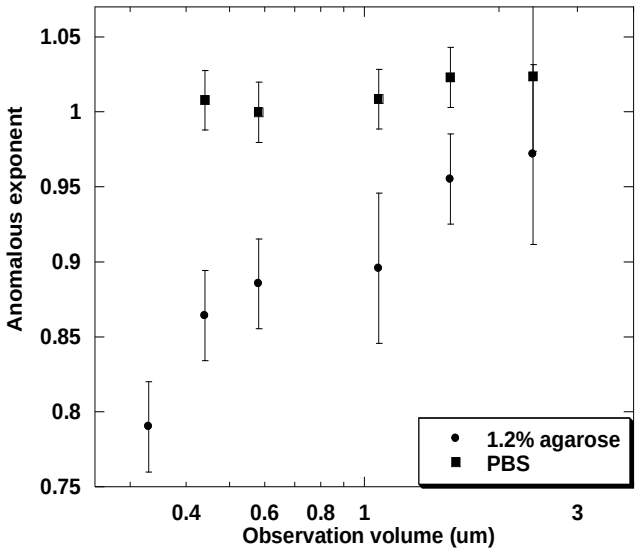

Figure 6 - The anomalous exponent as a function of observation volume for 40 nm beads suspended in 1.2% agarose gel and PBS solution.

The values for the anomalous exponent were obtained through fitting of the correlation functions recorded at different observation volumes. The beads in 1.2% agarose gel display anomalous behaviour while the beads in PBS display simple diffusion.

Banks, D., (2008)

It is clear that the PBS data shows little deviation from simple diffusion as α is approximately 1 at all length scales. On the other hand, the beads in agarose gel are illustrating anomalous behaviour through the decrease of α from ~1 to ~0.78 with the decrease of the observation volume. At longer length scales the exponent is about 1within error and hence the system seems to exhibit normal diffusion. This sort of behaviour can be explained using the idea of a cross over between two situations; one where the bead is freely diffusing and one where it is trapped. This trapping occurs because the agarose gel forms a network of cross-links or a mesh that the bead can get trapped in only if the size of the bead is comparable to the size of the mesh. In 1.5% agarose gel, the mesh size is predicted to be about 77 nm (Fatin-Rouge et. al., 2004), for 1.2% agarose gel this size would be slightly larger but still the same order of magnitude as the size of the bead. In this case, if the mesh is being observed with a very large detection volume, analysis of the correlation function implies that the bead is diffusing normally but very slowly. This gives rise to an effective diffusion coefficient that averages over the trapping and diffusing behaviour as if the medium is isotropic and just more viscous. With smaller

observation volumes, the correlation function does not fit a simple diffusion model and can only be explained using anomalous diffusion with a diffusion time faster than the one predicted with larger observation volumes. This points to the conclusion that it is the trapping that is overall reducing the transit time, not a slower rate of free diffusion. This technique has so far proven to give some valuable insight into the dynamics of this system but what we observe here is the upper edge of the cross over regime and limitations arise due to the diffraction barrier. Observation volumes that are the size of the mesh, <100 nm, would ideally help us understand exactly what is happening and extract information such as diffusion times and values of α at those length scales. We predict that at sub-diffraction length scales we would observe a VLS-FCS diffusion power law.

$$\langle w_o^2 \rangle \propto \tau_D^{\alpha}$$

This law states that the mean square displacement scales non-linearly with diffusion time, with α as the anomalous exponent that stays constant. At the diffraction limited length scales studied in this experiment (figure 6), the data does not complement this law since the value of α keeps decreasing. When $\langle w_o^2 \rangle$ is plotted against τ_D (from fits) to test for the diffusion power law, a value of α is extracted that is an average of the α values from figure 6. We believe that at sub-diffraction length scales the value of the anomalous exponent obtained from fitting the correlation functions would be a constant for all length scales and lower than what is obtained at the current length scales, which would validate the diffusion power law. This is the primary motivation behind building the STED instrument.

CHAPTER 2

Methodology

2.1 Set-up for STED-FCS

Our home built STED-FCS instrument is based on an inverted Nikon Eclipse Ti (Nikon, Japan). The STED set-up is based on a similar set-up reported in 2008 by B. Rankin et al., where they used 442 nm excitation and 532 nm STED pulsed laser sources with an average STED power between 24-162 µW. The dye they used was ATTO 425 and achieved a lateral resolution between 70-80 nm (Rankin, B et al., 2008). Figure 7 shows a schematic of our set-up, and the following is a description of each element and its function.

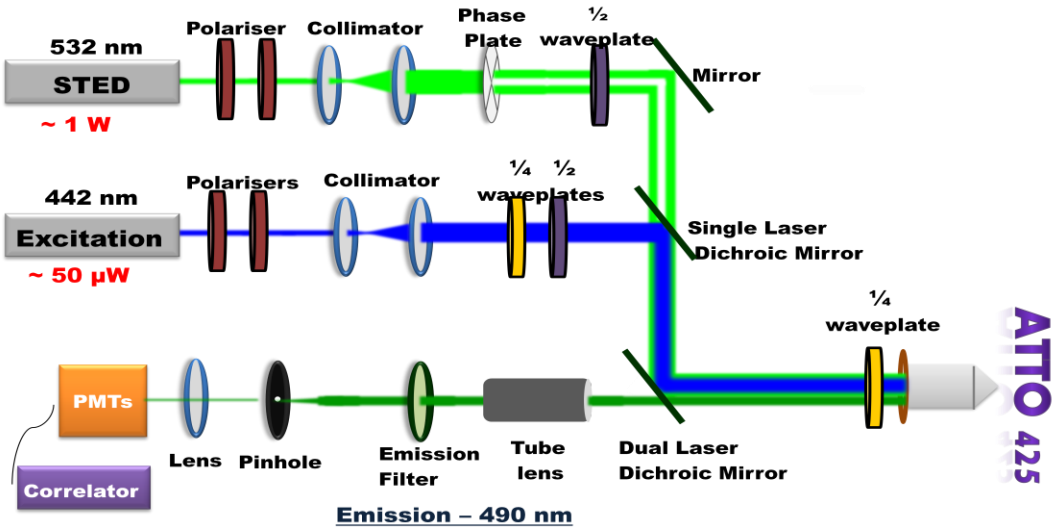

Figure 7 - Set up for the home built STED-FCS microscope
The 532 nm STED beam was vertically polarized and then collimated using a beam expander. It was then subjected to a 2π phase shift using a vortex phase plate. Before coming in contact with the dual laser dichroic mirror it was horizontally polarized using a 1/2 waveplate. A 1/4 wave plate was used to render it circularly polarized before entering the back aperture of the objective lens. The 442 nm excitation beam was also horizontally polarized using a 1/2 waveplate and then directed into the objective lens after passing through a 1/4 waveplate. Both beams were focused onto a sample containing the dye ATTO 425 (Figure 8b), the emission was then sent through an emission filter (D480/30M, Chroma Filters), then through a pinhole and finally focused onto a set of PMTs using a lens. The signal was then sent into a hardware correlator which correlated the data for FCS measurements.

a. *Diode-pumped Coherent Verdi-V10 laser* - This is a continuous wave light source with a wavelength of 532 nm. The beam comes out of the laser head vertically polarized and has a capacity of reaching a power of 10W. This laser is used for the quenching and will be called the STED laser.

b. *Glan-Laser calcite polarizer, Newport Corporation (STED)* - Two of these polarizers are placed directly in front of the STED laser and together they both control the output power and impart clean vertical polarization to the beam. The purpose of the first polarizer is to control the beam power and the purpose of the second polarizer is for ensuring that the beam has pure vertical polarization.

c. *Beam expander/collimator (STED)* - The beam expander comprises of a set of plano-convex lenses. The magnification is determined by the ratio of the focal distance of the two lenses. The first lens is LA1608A (Thorlabs-Inc.) with a focal distance of 75mm and the second is LA1433A (Thorlabs-Inc.) with a focal distance of 150 mm. The beam initially has a diameter of 2.25 mm ±10% and is expanded to a diameter of 4.5mm±10%. This is done by ensuring that the physical distance between the two lenses is the sum of their focal lengths.

d. *Vortex phase plate, RPC Photonics (STED)* - The phase plate is one of the most important optical components of the instrument and is responsible for creating the doughnut beam profile. This is achieved through the specific design of the plate itself. It is produced by lithographic techniques and has a continuous surface relief with the total height corresponding to the wavelength of interest. When circularly polarized

light travels through the phase plate it acquires a helical shape with a phase singularity in the centre around which the phase changes by a multiple of 2π. It should be noted that at this point the light is not circularly polarized but will be at a later point in the set up. Optical vortexes have a topological charge associated with them, which defines the number of twists the light does around its axis in one wavelength. For creating the torus shape, a phase plate of charge 1 is used, implying that the light twists once around its axis per wavelength.

e. *Half wave plate - zero order 532 nm, Edmund Optics (STED)* - A wave-plate is an optical device that modifies the polarization of the light wave passing through it. This is achieved through a controlled phase shift between the two orthogonal polarization components of the light wave. When travelling through the plate, the component of the light wave parallel to the optical axis of the wave-plate travels slightly slower than the one that is perpendicular such that it is exactly half a wavelength delayed. This results in a wave that is of the orthogonal polarization as compared to the original state. In our case, the beam is initially vertically polarized, but after passing through the half-wave plate it becomes horizontally polarized. Caution has to be taken to ensure that the fast or slow axis of the half wave plate is placed at a 45^{o} angle to the vertical. We believe converting the polarization of the STED laser from vertical to horizontal ensures a cleaner reflection at the dichroic mirror that directs the light into the objective.

f. *Liconix 300 series HeCd Laser* - This is a 442 nm continuous wave light source that is used for the excitation of the fluorescence in the sample. The light exits the laser head vertically polarized with a beam diameter of 1mm.

g. *Linear Polarizers, Newport Corporation (Excitation)* - Two linear polarizers are placed directly in front of the laser head, where the first controls the power and the second imparts vertical polarization. These polarizers have a much lower extinction ratio compared to the Glan-Laser Calcite polarizers. This is because the polarization plays a more significant role in the STED beam than it does in the excitation beam.

h. *Beam expander/collimator (Excitation)* - The first lens is LA1131-A (Thorlabs-Inc.) with a focal distance of 50 mm and the second lens is LA1708-A (Thorlabs-Inc.) with a focal distance of 200 mm. This gives a magnification of 4 resulting in a beam width of 4 mm.

i. *Half wave-plate - zero order 442nm, Edmund Optics (Excitation)* - Converts vertically polarized light into horizontally polarized light.

j. *Single laser dichroic mirror - z442rdc, Chroma Technology Corp.* - This dichroic mirror reflects 442 nm wavelength and transmits all wavelengths beyond that up to 748 nm including the STED wavelength of 532 nm. This is an integral piece of the set-up since it permits combining the two laser beams (Figure 8a).

k. *Dual laser dichroic mirror - Z442/532rpc, Chroma Technology Corp.* - This mirror reflects the wavelengths 442 nm and 532 nm directing them into the back aperture of the objective lens while transmitting all other wavelengths (Figure 8a).

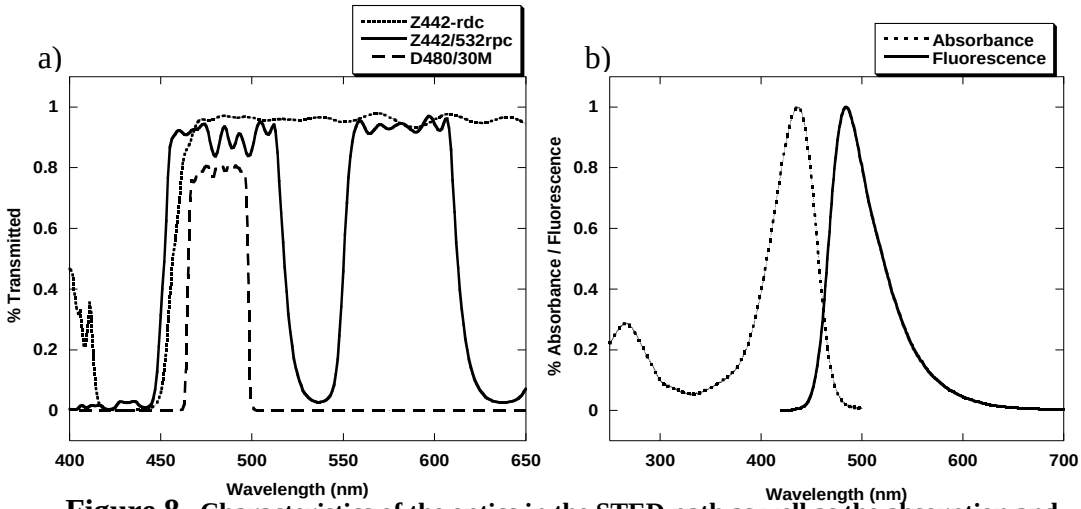

Figure 8 - Characteristics of the optics in the STED path as well as the absorption and emission spectra of the dye ATTO 425

a) Wavelength transmittance for the single laser dichroic mirror, Z442rdc (NC191968 - z442rdc, Chroma Tech. Corp., 2012), the dual laser dichroic mirror, Z442/532rpc (NC282471 - z442/532/633rpc, Chroma Tech. Corp., 2012) and the emission filter, D480/30M (D480/30m, Chroma Tech. Corp., 2012). b) Absorbance and fluorescence properties of the dye, ATTO 425 (ATTO 425/Spectra_XLS, ATTO-TEC, 2012).

l. *Achromatic quarter wave-plate, Edmund Optics* - A quarter wave-plate is placed right before the objective lens in order to impart circular polarization to the STED and excitation beams. As mentioned before it is essential to have circular polarization in order to obtain a symmetric doughnut profile with a zero intensity point on the optical axis. The principle behind a quarter wave-plate is similar to a half-wave plate except one component of the light is a quarter wavelength behind the other, resulting in an electric field vector that is constantly changing direction if the light was initially linearly polarized. Again, in order to get clean circular polarization, it is crucial to keep the axis of polarization (horizontal, in this case), at an angle of 45^{o} with respect to the fast/slow axis of the wave-plate. A good test for circular polarization is to place a

polarizer after the quarter wave plate and rotate it to check for a constant intensity signal.

m. *Plan Fluor Oil immersion objective lens, Nikon, Japan* - The objective lens used to focus the beams is an oil immersion with a numerical aperture of 1.3 and a magnification of 100X. The same lens is used to collect the fluorescence light from the excitation spot which is then sent to the detectors.

n. *Emission filter- D480/30M, Chroma Techonology* - The combination of the excitation and STED lasers allow a limited number of fluorescent probes to be examined. The dye that was used in this set-up is ATTO 425 (ATTO-TEC, Germany), which can be excited efficiently in the range 405-455 nm and emits at 484 nm (Figure 8b). Hence, an emission filter with ~80% transmission in the range 450 nm to 510 nm was used, which effectively blocks the excitation wavelength of 442 nm and the STED wavelength of 532 nm, which is absolutely essential for STED to work (Figure 8a).

o. *Photomultiplier tubes-H7421 Series, Hamamatsu Photonics, Japan* - Two of these photon counting heads were utilized for detecting the fluorescence emission. The emission, after passing through a pinhole, was focused into a polarizing beamsplitter (Newport Corporation) using a lens and the split beams were directed into the PMTs. The large detection windows of the PMTs allows easier alignment of the emission beam. Other advantages of PMTs include high sensitivity and a high speed response time. Due to their high sensitivity the detectors were encased in a black cardboard box.

p. *Correlator - Flex02-01D, Correlator.com, China* - Flex02-01D is a photon counting digital hardware that functions as a single high resolution MT-64 multiple tau digital correlator. The multiple tau is a semi-logarithmic correlator scheme where the sample time doubles every 32 channels. The correlation time is proportional to the sample time, hence a wider range of correlation times can be covered with the same number of channels as a linear correlator. The minimum sample time that is required for this instrument is 1.5625 ns and it calculates the correlation function in real time with delay times (or lag time) of 1.5625 ns to 30 minutes.

2.2 Pinhole alignment

A pinhole alignment routine which automatically locates the best pinhole position in the x, y and z direction was written in Labview (National Instruments,). The purpose of the routine is to ensure the most accurate pinhole position is obtained which should result in the highest possible intensity signal and the highest possible count per particle. The algorithm for this routine is as follows:

Z-SCAN

The Z-SCAN basically scans for the position in the z axis (optical axis) where the emission is focused by the tube lens in the microscope. Placing the pinhole right at the focus gives the optimal intensity signal. At each z position, the x and y directions were scanned for the highest count. The routine for the x-y scan is described below.

- At the first z position a wide x-y scan is performed since the pinhole may be far from the best position in the x-y plane. In this case the user is required to give the

initial direction for the movement of the x and y motors. The x motor then moves 10,000 units (~ 3.25 μm travel/300 units, see section 2.2.1) in the negative direction (in case the pinhole was close to the peak intensity) and then takes 10 steps in increments of 3000 units in the positive direction scanning over the peak and arriving on the other side. Here positive refers to the direction of travel that increases intensity and negative to the direction that decreases it. The intensity values at every step are recorded and the motors then travel back to the point with the highest intensity. The same is done for the y motors. After this initial scan, the motors again scan over the peak sequentially in increments of 2000, 1000, 100 and 50 units until the best pinhole position is obtained in both directions.

- For the remainder of the z positions, a narrow x-y scan is done since the pinhole is generally in the vicinity of the peak intensity. For this scan, the direction of travel for both x and y is chosen automatically based on whether the intensity drops or increases by moving in a certain direction. Once the correct directions are known, the above procedure is repeated with just smaller units of increment since it is a narrow scan.
- At every z position the final peak intensity is recorded and after all the z scans are finished, the motors move to the best z position and the x-y scan is performed again.

2.2.1 Calibration of the pinhole motors (Newport Corporation, USA):

Materials:

- 60X magnification objective lens (Nikon, Japan)
- Calibration slide (Graticules Pyser-SGI Ltd.)
- Adjustable iris
- Camera

Method:

The calibration slide (50 divisions, 2 µm spacing) was illuminated using bright field illumination and the resulting image was viewed on a camera placed right after the pinhole mount. Since a 60X magnification objective lens was used, the magnification at the pinhole is 60X resulting in an increment size of 120 µm. An iris was mounted onto the pinhole mount and the calibration slide was centred so it could be viewed through the iris onto the camera. The motors were then moved in the y direction in increments of 300 units till a distance of 120 µm was covered. About 37 steps were required to cover this distance resulting in an approximate rate of travel of 3.25 µm/300 units.

2.3 Alignment of the pinhole and visualization of the doughnut/Gaussian profiles using a camera

For the purposes of imaging or taking FCS measurements it is essential to visualize the doughnut/Gaussian profile before hand to check for symmetry and overall quality. This could be done by using a camera (Moticam 1000, Motic, Canada) which can be placed after the pinhole. In order for the camera to capture any photons after the pinhole, the intensity of the STED laser should be increased to about 1 W from the control knob and a higher concentration of the dye should be used, 1µM. The FCS measurements for the

doughnut and Gaussian detection volumes were taken using the dye, ALEXA Fluor 532 (Invitrogen, Life Technologies), since it is excited by the STED wavelength of 532 nm. In order to achieve a symmetric doughnut profile, first a 100 µm pinhole was aligned for the Gaussian profile using the detectors and then the phase plate was positioned in the STED path to obtain the doughnut. One can then view the doughnut focal spot on the camera monitor and align the pinhole with the centre of the doughnut. Generally, the pinhole alignment routine does a good job of aligning the doughnut, but it is good practice to view the doughnut on the camera monitor before imaging because if the doughnut is not symmetric and tends to have a higher intensity on any one side, then the alignment routine could favour that side and the alignment would be slightly off. This is generally only a problem with pinhole sizes 50 µm or smaller.

2.4 Imaging

For confirming the shape of the doughnut and Gaussian illumination profiles, 0.04 µm fluorescent beads (Invitrogen, Life Technologies) were imaged at the STED wavelength.

Sample preparation: 40 nm latex beads made from polystyrene and loaded with fluorescent dye with excitation/emission at 540/560 nm were obtained (Invitrogen, Life Technologies). The beads were first diluted to a concentration of 50 nM (see section 2.4.1) using PBS in an Eppendorf tube and then vortexed thoroughly to avoid aggregation. Then using a micropipette about 50 µL solution was transferred onto a home-made micro-chamber which was then sealed using candle wax. Since these beads have an affinity for glass they tend to attach themselves to the cover glass of the micro-chamber and hence can be easily imaged in that plane. The chamber was then placed on a

piezo stage for scanning of the sample. A fluorescent mercury lamp (Nikon, Japan) with a green excitation filter was allowed to illuminate the sample and the fluorescing beads could be located using a camera. The particular bead chosen for imaging, generally a bright one, was moved close to the focused excitation spot by moving the chamber itself or the stage and the sample was ready for imaging.

Imaging: A program that controlled the movement of the scanning stage as well as formed a pseudo colour image of the illumination profile was written in LABVIEW. The user was first required to input the absolute position of the stage in x and y as well as the desired dimension of the image (x *y) and the step size. For this particular scanning stage, the step sizes can range from 1 µm to 1 nm. After inputting these quantities, the bead scanned over the illumination spot from left to right in x till it had scanned y rows. At each step the intensity was recorded and a pseudo image was formed row by row. The preferred step sizes for acquiring the details of the illumination profile and being able to see a clear intensity minimum at the centre is ~ 20 nm to 50 nm. These beads are quite photo-stable and hence a single bead can be scanned an average of four times before it starts to photo-bleach.

2.4.1 Determining concentration of 40 nm orange beads

The number of microspheres per mL can be determined using the equation:

$$Number\ of\ \frac{microspheres}{mL} = \frac{6C\ \times 10^{12}}{\rho \times \pi \times \phi^3}$$

The 0.04 µm fluorospheres are supplied as aqueous suspensions with 5% solid and hence the concentration is 0.05 g/mL. The density of polymer in g/mL is 1.05 for polystyrene and the diameter of the beads in µm is 0.04 resulting in:

$$Number\ of\ \frac{microspheres}{mL} = \frac{6 * 0.05\frac{g}{mL} \times 10^{12}}{1.05\frac{g}{mL} \times \pi \times 0.04^3} = 1.42 \times 10^{15}$$

This is equivalent to a stock concentration of ~2.36 x 10^3 nM.

2.5 Alignment of STED and excitation beam

Fluorescence depletion by the STED beam can only occur if it is completely superimposed onto the excitation beam at the focal spot. Hence, alignment of the two beams is an important step in the set-up process. It is easier to superimpose the two beams in the x and y directions using the camera right after the pinhole. A mix sample comprised of the dyes ATTO 425 and Alexa Fluor 532 was prepared which would enable excitation by both lasers simultaneously. The emission filters were removed so that neither emission would be blocked. The 50 µm pinhole was aligned with one of the laser's emission and then the second beam was aligned with the pinhole by manually adjusting the mirrors. Alignment in the z direction, or the axial plane, would enable both beams to focus at the same spot on the sample which is essential for complete quenching of the sample. This is a bit more tricky and requires alteration to the collimation of the beam being adjusted. By changing the distance between the lenses in the beam expander, the beam's width can be altered and this affects how far it is focused by the objective lens. In

theory overall alignment of the two beams seems attainable but it is harder to actually do and hence a more quantitative and sensitive method for alignment is needed and will be discussed later in the results and discussion section.

2.6 Using FCS to study properties of the STED doughnut

One of the major hindrances in the building and performance of a STED microscope is the quality of the STED doughnut obtained. Proper alignment of the beam with the phase plate, the objective lens, and the pinhole determine the quality of the doughnut. Here, quality refers to an isotropic ring-shaped intensity profile around a central zero intensity minimum. We propose a new method to test the characteristics of a doughnut based on FCS. We calculated the model mathematical function associated with the correlation function of a doughnut shaped beam by approximating the doughnut as a subtraction of two Gaussians (Appendix B). In FCS, excitation beam alignment quality can be assessed based on specific brightness, hence we suggest here that the same can be done for the STED beam alignment.

CHAPTER 3

Results and Discussion

3.1 Calculated point spread functions with and without a phase plate

The intensity near the focus for any given illumination profile can be calculated from the expression of the electric field near the focus. The electric field at the cylindrical coordinate (r,z,φ) can be calculated from vectorial diffraction theory using the polarization state of the incident field, P(θ,ϕ), the semiaperture angle, α, the refractive index, n, and the light wavenumber, k (Tian, B. and Pu, J., 2011):

$$E(r,z,\varphi) = iC\int_0^{\alpha} d\theta \int_0^{2\pi} \sqrt{cos\theta}\, sin\theta P(\theta,\phi) e^{[ikn(zcos\theta + rsin\theta)\cos(\phi-\varphi)]}\, d\phi \qquad [3.1]$$

The complex polarization state P(θ, ϕ), describes the phase information due to the presence of the phase filter in the case of the doughnut. θ is the inclination angle and ϕ is the azimuth angle between the polarization direction of the of the light rays exiting from the lens and the observation plane.

The focal intensity is then written as:

$$I(r,z,\varphi) = I_0 |E(r,z,\varphi)|^2 \qquad [3.2]$$

Carrying out the integration in equation 3.1 numerically (using Mathematica) and using a constant phase parameter, $P(\theta,\phi) = e^{i*0} = 1$, for n = 1.5, k = 2π/532 nm^{-1}, α=60^{o} and z = 0, yields a diffraction limited PSF, also known as an Airy pattern shown in Figure 9 (solid circles).

The modulation of the phase introduced by the vortex phase plate is indicated by $P(\theta, \phi) = e^{i\phi}$ and when inserted into equation 3.1 gives a PSF with a doughnut profile as also shown in Figure 9 (open circles).

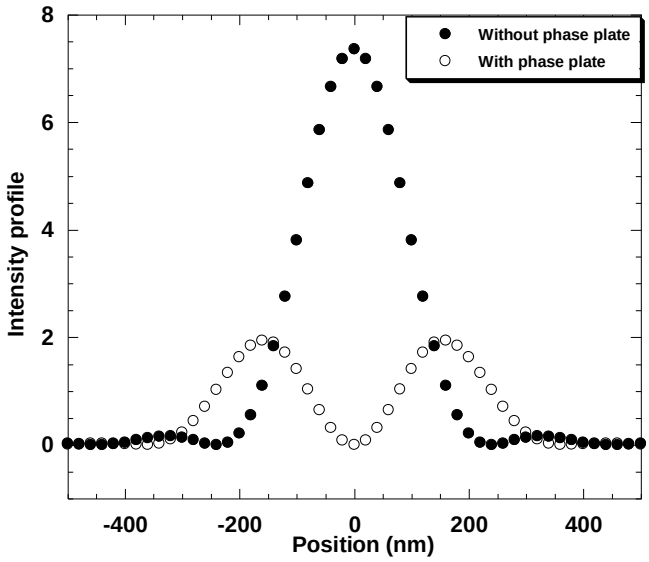

Figure 9 - Calculated point spread functions with (open circles) and without (solid circles) a phase plate.

The profiles were calculated using Mathematica for n = 1.5, k = 2π/532 nm^{-1}, α=60° and z=0.

According to Figure 9 we expect spreading of the light intensity of the doughnut profile in comparison to the Airy disk as well as quite a significant decrease in maximum intensity. If the doughnut is completely symmetric as shown by the calculations then at no point in space should it have an intensity higher than the maximum intensity of the Airy disk. In fact according to the intensity profile generated in Figure 9 the maximum doughnut intensity should be about a quarter of the maximum Airy disk intensity.

3.2 Gaussian approximation of the calculated profiles

The calculated PSF for an Airy disk (without phase plate) can be approximated with a two dimensional Gaussian (Zhang et. al., 2007):

$$I_G(x,y) = I_{o,G} e^{\frac{-2x^2}{\omega_0^2}} e^{\frac{-2y^2}{\omega_0^2}} \quad [3.3]$$

$I_{0,G}$ is the maximum intensity and a least-square fit of the profile in Figure 9 using the simple Gaussian approximation yields in this case the $1/e^2$ half width, ω_0, of 167±1 nm (Figure 10a). The FWHM is equal to $\sqrt{2ln2}\,\omega_0$ and for the value of ω_0 given it is calculated to be 196.7 nm. From equation 1.1, with λ = 532 nm and NA = 1.3, the expected value of FWHM is 208.7 nm. According to the residuals shown in Figure 10a the fit seems to get worse at the edges which is expected since the actual profile is an Airy pattern which is comprised of a series of concentric bright rings around the Airy disk. Hence the Gaussian approximation is not ideal for modelling the detection volume in FCS and is only a reasonable approximation very close to the focus (Hess, S. and Webb, W., 2002). Nevertheless it is a good enough fit for our purposes and we will continue to use it to approximate the PSF of the Airy pattern as it is normally done for FCS measurements.

To further explore the characteristics of the doughnut illumination profile (with phase plate) it is imperative that we generate a function that can represent it relatively well and is easy to work with. Here, we propose the difference of two Gaussian functions as an approximation to the doughnut shape.

The function that we therefore used to fit the phase modulated data in Figure 9 is:

$$I_D(x,y) = I_{0,D}\left[e^{\frac{-2x^2}{\omega_2^2}} e^{\frac{-2y^2}{\omega_2^2}} - e^{\frac{-2x^2}{\omega_1^2}} e^{\frac{-2y^2}{\omega_1^2}}\right] = I_{0,D}\left[e^{\frac{-2r^2}{\omega_2^2}} - e^{\frac{-2r^2}{\omega_1^2}}\right] \quad [3.4]$$

Here $I_{0,D}$ is the amplitude of the two Gaussian functions which is the same since the intensity at the centre of the doughnut is zero.

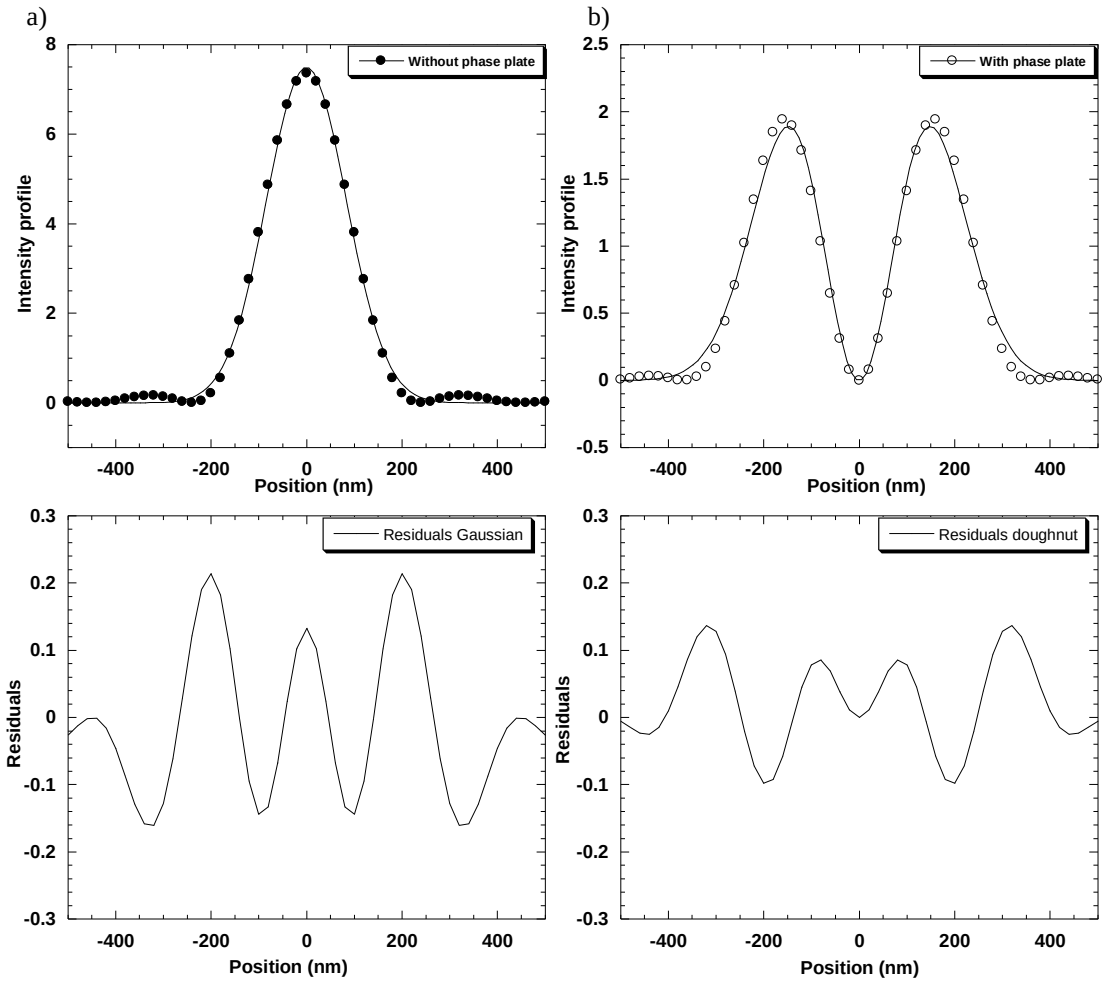

Figure 10 - **Fits of numerically calculated point spread functions for the Airy disk and doughnut profile using a Gaussian approximation.**

a) Simple Gaussian approximation fitting of the Airy disk. We obtain ω_0 = 167.1 nm and corresponding residuals, χ^2 = 0.62. b) Difference of Gaussian fit of the doughnut profile, giving ω_2= 213.44 nm and ω_1 = 207.54 nm and corresponding residuals, χ^2 = 0.24.

Using equation 3.4 with the two widths as the fitting parameters we were able to get a relatively good fit of the numerically calculated doughnut profile in Figure 10b with a chi-square value of ~ 0.24. In comparison, the chi-square value for the Gaussian approximation (Figure 10a) is ~ 0.62. According to the residuals in Figure 10b the fit seems to get worse at the outer edges of the doughnut which is expected since the

doughnut just like the Airy pattern possesses secondary minima away from the optical axis. In this case, the width of the wider Gaussian function, ω_2, is 213±100 nm and the width of the narrower function, ω_1, is 207±100 nm. The ratio ω_2/ω_1, which can also be referred to as σ is 1.03±0.9. The huge error in σ means that there are various combinations of ω_2 and ω_1 that can fit the doughnut profile, but the fit for the above mentioned widths gives the lowest chi-square value.

The maximum intensity for the Gaussian profile, $I_{0,G}$ can be related to the net power, P_0, radiating from the source which is a constant:

$$P_0 = \int I_G dA \qquad [3.5]$$

By substituting equation 3.3 into equation 3.5 we get:

$$P_0 = \iint dxdy\, I_{0,G}\, e^{\frac{-2x^2}{\omega_0^2}}\, e^{\frac{-2y^2}{\omega_0^2}}$$

$$P_0 = I_{0,G}\, \frac{\pi\omega_0^2}{2}$$

Hence, the maximum Gaussian intensity is:

$$I_{0,G} = \frac{2P_0}{\pi\omega_0^2} \qquad [3.6]$$

Likewise, by substituting the function for the doughnut profile in equation 3.4 into equation 3.5 we can calculate the maximum doughnut intensity, $PSF_{max,D}$.

$$P_0 = \iint dxdy\, I_{0,D} \left[e^{\frac{-2x^2}{\omega_2^2}}\, e^{\frac{-2y^2}{\omega_2^2}} - e^{\frac{-2x^2}{\omega_1^2}}\, e^{\frac{-2y^2}{\omega_1^2}} \right]$$

$$P_0 = \frac{\pi I_{0,D}}{2} [\omega_2^2 - \omega_1^2]$$

This gives us the expression for $I_{0,D}$:

$$I_{0,D} = \frac{2P_0}{\pi(\omega_2^2 - \omega_1^2)} \qquad [3.7]$$

In the focal plane, the maximum PSF intensity for the Gaussian, $PSF_{max,G}$, occurs at r = 0 and is equal to $I_{0,G}$. For the doughnut, $PSF_{max,D}$ can be calculated by first determining the position r at which the maximum in intensity occurs. Calculating the derivative of $I_D(r)$ with respect to r we get:

$$\frac{dI_D(r)}{dr} = \frac{-4r}{\omega_2^2} e^{\frac{-2r^2}{\omega_2^2}} + \frac{4r}{\omega_1^2} e^{\frac{-2r^2}{\omega_1^2}} = 0$$

$$r_{max,D} = \frac{\omega_1 \omega_2 \sqrt{log \frac{\omega_2}{\omega_1}}}{\sqrt{\omega_2^2 - \omega_1^2}} \qquad [3.8]$$

Hence $PSF_{max,D}$ is:

$$PSF_{max,D} = I_{0,D} \left[\left(\frac{\omega_2}{\omega_1} \right)^{\frac{-2\omega_1^2}{\omega_2^2 - \omega_1^2}} - \left(\frac{\omega_2}{\omega_1} \right)^{\frac{-2\omega_2^2}{\omega_2^2 - \omega_1^2}} \right] \approx 0.0206 I_{0,D}$$

The ratio $\frac{I_{0,D}}{I_{0,G}}$ is about 11.2 which makes $PSF_{max,D} \approx 0.23 PSF_{max,G}$. The ratio between $PSF_{max,D}$ and $PSG_{max,G}$ measured from the intensity data values in Figure 9 is ~ 0.25. The fact that the value obtained from the calculated profiles (Figure 9) is so close to the value calculated from the Gaussian fits shows that the double Gaussian approximation with σ~1 is a good approximation of the theoretical doughnut profile.

To show further that the σ~1 is a good approximation we can also calculate $r_{max,D}$ (equation 3.8) and compare it to the doughnut profile obtained in Figure 10. We rewrite equation 3.8 in terms of σ=1+ε, where ε<<1.

$$r_{max,D} = \frac{\omega_2 \sqrt{log \sigma}}{\sqrt{\sigma^2 - 1}} = \frac{\omega_2 \sqrt{\log (1+\varepsilon)}}{\sqrt{\varepsilon^2 + 2\varepsilon}}$$

For small ε the expansion of the natural logarithm log(1+ε) is $\varepsilon - \varepsilon^2/2$. Using that in the above expression:

$$r_{max,D} \approx \frac{\omega_2\sqrt{\varepsilon(1-\frac{\varepsilon}{2}}}{\sqrt{2\varepsilon(\frac{\varepsilon}{2}+1)}} \approx \frac{\omega_2}{\sqrt{2}}$$

Based on the value of ω_2 obtained, 213.44 nm, the position of the doughnut with the maximum intensity $PSF_{max,D}$ is 150.9 nm. In Figure 10, the measured maximum intensity for the doughnut occurs at a radius of about 150 nm which is in excellent agreement with the calculated value, reinforcing the argument that $\sigma \sim 1$ is valid.

3.3 Measured intensity profiles

In order to test the quality and alignment of the incoming beam, images of the regular Gaussian excitation spot were taken using 40 nm beads that absorb at 532 nm. A representative image as well as a profile taken along a particular direction and integrated radial profile are shown in Figures 11a,b,c.

Figure 11a shows the diffraction limited PSF formed with a Gaussian beam and the fit obtained in Figure 11b along the axis shown gives ω_0 equal to 272.18 nm. Figure 11c shows the radial profile for the image, which was obtained by integrating the intensity along concentric circles of increasing radius from the centre which was determined using ImageJ.

At a radius of 0 nm we have the point of highest intensity at about 42.7 kHz and this plot was also fitted with a Gaussian function and resulted in a width of 224.7 nm. This value is closer to the calculated value of 208.7 nm from equation 1.1 and will be used in the future since it gives more information about the image as compared to the profile along a line.

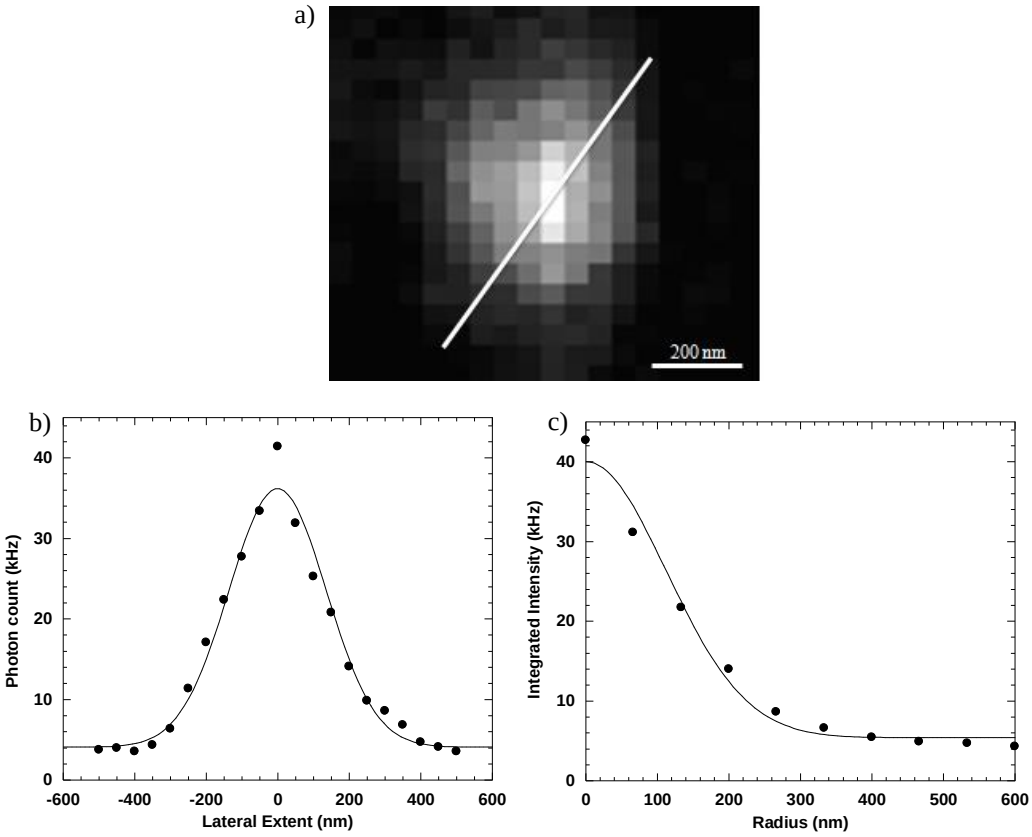

Figure 11 - **Experimentally obtained intensity profile for the Gaussian Illumination**
a) Image of a Gaussian focal spot. The line across shows the axis along which the intensity profile was obtained. b) Intensity profile along the line shown in a) fit with a Gaussian function; ω_0 = 272.18 nm. c) Integrated radial profile fit with a Gaussian; ω_0 = 224.7 nm.

224.7 nm is also an increase of 34% when compared to ω_0 obtained from the calculated profile in figure 9 (ω_0=167.1 nm). Firstly, this increase in size could be the result of optical aberrations of the objective lens because of which expected ω_0 based on NA are always underestimated compared to the actual ω_0 obtained. Secondly, the increase in size could be the result of the beam not being completely focused onto the glass cover slip on which the bead was attached during the scan. The reason for this is that the beads were first viewed and brought into focus using a fluorescence lamp which may not necessarily

have the same focal plane as the laser beam. Also Equation 3.1 which was used to generate the theoretical profiles tends to underestimate the size of the focal spot since it assumes that no interfaces are present in the light path after the objective lens while in the actual experimental set-up there is the cover slip. Finally, the calibration of the piezo stage that was used for scanning the sample also plays an important role and if the calibration was slightly off that could affect the scale shown in the image.

Optimizing of the doughnut illumination profile is easier to do if images of the doughnut at different stages of alignment are accessible. Figure 12a shows the image taken by scanning the bead over the doughnut focal spot and a resulting intensity profile and integrated radial profile are shown in Figures 12b,c and d respectively.

Figure 12a shows a clear central region of minimum intensity as is expected for a doughnut shape. The centre of mass for the image when calculated with ImageJ was found to correspond to the centre of the dark spot indicating that the doughnut is reasonably symmetric. The intensity around the ring however is concentrated in some areas more than others. This artifact seems mainly due to the specific design of the phase plate which does not allow even distribution of the light rays upon focusing. A physical region of reduced intensity travelling from the central dark spot radially can be seen in all images of doughnut obtained. In figure 12a it can be seen on the left side of the image along the horizontal axis. This line is also present on the phase plate (marking the start of the helix pattern) and it is unclear whether it is imprinting onto the focal spot due to possible misalignment of the phase plate, a faulty phase plate, non-perfect circular polarization or just low beam quality.

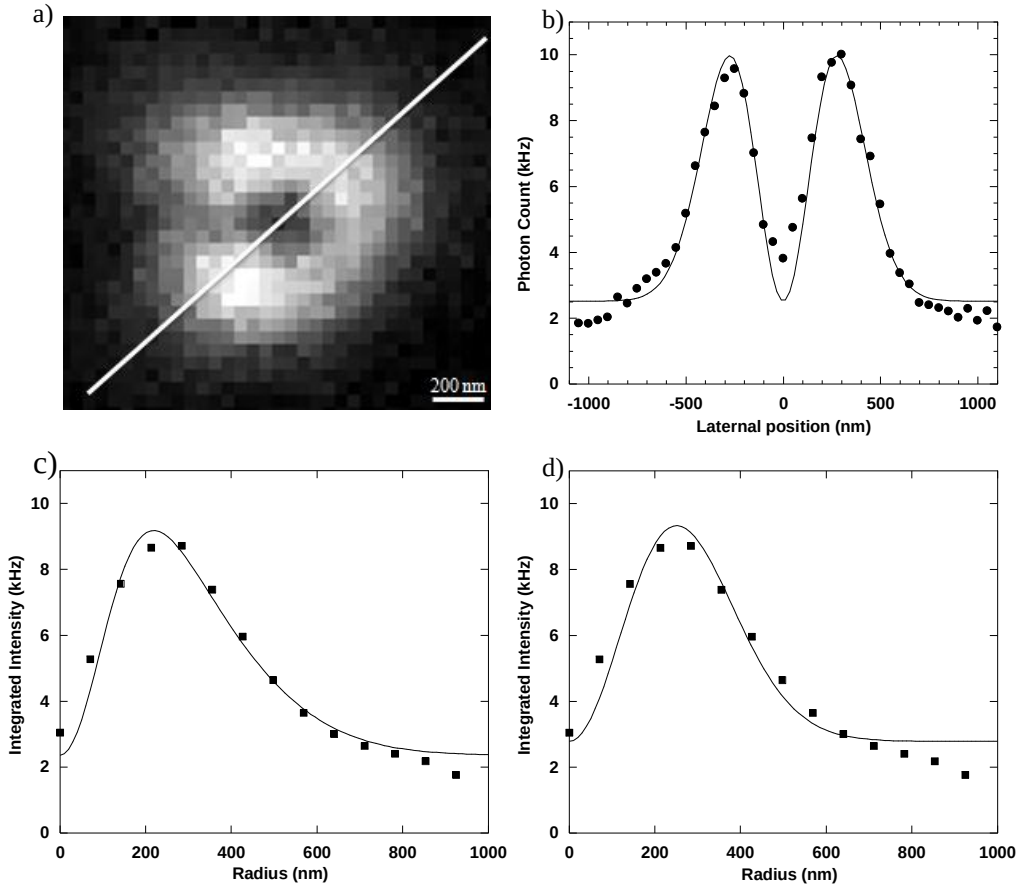

Figure 12 - Experimentally obtained intensity profile for the Doughnut Illumination

a) Pseudo-colour image of the doughnut focal spot was taken by scanning a 40 nm fluorescent bead over the focal spot and recording the intensity at each 50 nm step. The line across shows the axis along which the intensity profile was obtained. b) Linear intensity profile along the line shown in a) fit with a difference of Gaussian functions, ω_2 = 397.51 nm and ω_1 = 382.51 nm. c) Integrated radial profile of doughnut image obtained by integrating intensity along concentric circles of increasing radius. This was also fit with a difference of Gaussians with ω_2 = 567.78 nm and ω_1 = 201.16 nm. d) Integrated radial profile of doughnut image fit with a difference of Gaussians with ω_2 = 362.07 nm and ω_1 = 348.54 nm. The peak intensity was found around a radius of 210 nm.

In any case, having a doughnut with asymmetric intensity distribution can affect the resolution in STED and hence this problem needs to be addressed and should be rectified. In the meantime, the profile of the doughnut along the axis shown in Figure 12a was plotted using ImageJ and is shown in Figure 12b. The intensity at both peaks seems

reasonably symmetric and upon fitting with a difference of Gaussians the values for ω_2 and ω_1 came out to be 397.51 nm and 382.51 nm respectively with a chi-square value of 12.3. This yielda a ratio of 1.04, very close to the expected ratio of 1.03. Figures 12 c and d both show the integrated radial profile of the doughnut with different fit values based on the initial parameters. In Figure 12c, ω_2 and ω_1 obtained were 567.78 nm and 201.16 nm respectively. Both of these values are higher than the ones obtained from fitting the theoretical phase modulated data and their ratio of ~3 is also much higher than the expected ratio of 1.03. The fit in Figure 12d yields ω_2 and ω_1, 362.07 nm and 348.54 nm, respectively and their ratio, σ =1.04 is again very close to the expected ratio of 1.03. Both fits do a reasonably good job with fitting the doughnut peaks but the first fit seems to fit the outer edges of the doughnut better. Figure 12.1 shows the residuals for both fits (c and d).

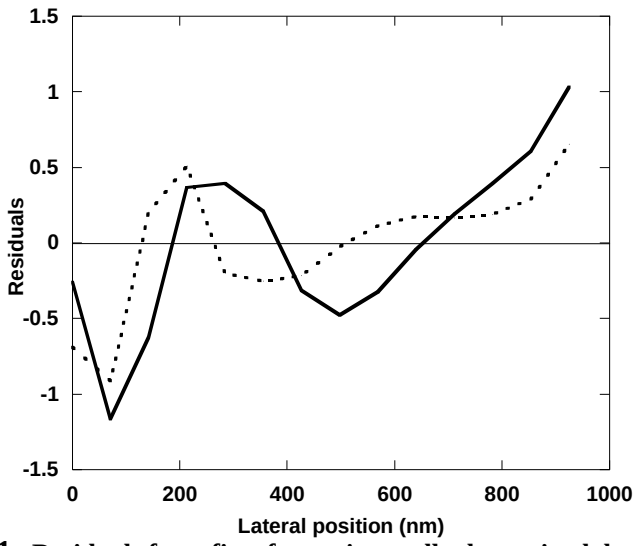

Figure 12.1 - **Residuals from fits of experimentally determined doughnut intensity profile using different initial values**

Dotted line: Residuals from the fit of Figure 12c with $\sigma \sim 3$. Solid line: Residuals from the fit of Figure 12d with $\sigma \sim 1.03$.

From Figure 12.1 we can see that the residuals for both fits are comparable till about the 400 nm point and past that the first fit is better (dotted). Since in an FCS experiment the pinhole blocks out the outer edges and we are mainly interested in fitting of the doughnut peaks we can reject the first fit and use the second fit (solid) which is closer to theoretical predictions. The fit parameters from this fit will be used to represent the PSF of the doughnut for reference in the future. Comparison between the doughnut profiles in Figure 9 and Figure 12b also show increased overall width in the experimentally determined doughnut profile, basically indicating a larger sized focal spot. The width between the maximum intensity points in the theoretical doughnut is about 300 nm whereas it is about 420 nm in the experimentally determined profile. This is an increase of about 40% and the same reasons apply here as they did for the Gaussian case. This is an indication that the experiments are consistent with each other and the previously mentioned reasons are the only anomalies in the experimental set-up. Lastly we do not see a central region of zero intensity in the experimentally determined doughnut profile in Figure 12b. First, since the zero spot in the centre is a point singularity and the bead has a width of 40 nm associated with it we may never be able to see a complete zero intensity point even though it is there. Each pixel on the image is 50 nm and in practice it is difficult to go to step sizes lower than that without losing intensity due to photo-bleaching because of repeated scans on the same bead. Second, it is most likely the case that a zero intensity minimum is only seen at the focus of the beam and if the image has been taken when it was off-focus it could also contribute to the non-zero intensity at the centre of the doughnut. Third, the background noise obtained from the image is about 2 kHz and the

intensity at the centre of the doughnut is 3.8 kHz. By subtracting the background we get a an intensity closer to zero. Regardless we do a see a quite a sharp decrease in intensity at the centre which is indicative of the presence of a doughnut. Even though different beads were scanned to obtain the doughnut and Gaussian images in Figures 11 and 12 it is interesting to see that the ratio of the maximum intensity between both is still about 0.25 as expected.

3.4 Autocorrelation function for a doughnut illumination profile

As we previously saw, the formation of the doughnut is accompanied by a spreading of the PSF as well as a reduction in peak intensity when compared to the Gaussian case. Both of these characteristics would affect the autocorrelation function of a doughnut profile to a great extent. Hence, we decided to measure autocorrelation functions for both Gaussian and doughnut profiles for different pinhole sizes to assess how the shape of the correlation curve is affected. We predicted that we would see a decrease in the height of the ACF and a larger characteristic time because of the enlargement of the focal spot.

3.4.1 Theory

The well known ACF for a Gaussian detection volume without the triplet state term (calculated in Appendix A) is:

$$G_G(\tau) = \frac{1/N_G\left[\frac{1}{\left(1+\frac{\tau}{\tau_{D,0}}\right)}\right]}{\sqrt{1+\frac{\tau}{S^2\tau_{D,0}}}} \qquad [3.9]$$

Now in order to back up our predictions about the doughnut ACF with theory we used the difference of Gaussians, $I_D(x,y,z) = I_{0,D}\left[e^{\frac{-2x^2}{\omega_2^2}} e^{\frac{-2y^2}{\omega_2^2}} - e^{\frac{-2x^2}{\omega_1^2}} e^{\frac{-2y^2}{\omega_1^2}}\right] e^{\frac{-2z^2}{z_0^2}}$ as the PSF in the autocorrelation function equation (equation 1 in Appendix A) to calculate a model correlation function for the doughnut profile.

We found the ACF (calculation shown in Appendix B):

$$G_D(\tau) = \frac{\frac{\omega_2^2}{\frac{4D\tau}{\omega_2^2}+1} + \frac{\omega_1^2}{\frac{4D\tau}{\omega_1^2}+1} - \frac{4\omega_2^2\omega_1^2}{8D\tau+\omega_2^2+\omega_1^2}}{\langle C\rangle \pi^{3/2} z_0 \left[\omega_2^2-\omega_1^2\right]^2 \sqrt{\frac{4D\tau}{z_0^2}+1}} \qquad [3.10]$$

The effective volume of the doughnut illumination profile can be calculated using the equation:

$$V_D = \iiint \left[e^{\frac{-2x^2}{\omega_2^2}} e^{\frac{-2y^2}{\omega_2^2}} - e^{\frac{-2x^2}{\omega_1^2}} e^{\frac{-2y^2}{\omega_1^2}}\right] e^{\frac{-2z^2}{z_0^2}} dxdydz$$

$$= \pi^{3/2} z_0 \left[\omega_2^2 - \omega_1^2\right] \qquad [3.11]$$

As a reminder, the effective volume of the Gaussian detection volume is:

$$V_G = \pi^{3/2}\omega_0^2 z_0$$

According to Equation 3.11 the effective detection volume for the doughnut is basically a difference of the volumes of two Gaussians which is not surprising.

The number of particles in the doughnut detection volume can be expressed as

$$N_D = \pi^{3/2} z_0 \left[\omega_2^2 - \omega_1^2\right] \langle C \rangle \qquad [3.12]$$

Note that $G_D(0)$ is not equal to $1/N_D$ as it was in the case of the Gaussian, but instead $G_D(0) = \frac{1}{\langle C \rangle \pi^{3/2} z_0 [\omega_2^2 + \omega_1^2]}$. Inputting equation 3.12 into equation 3.10 and simplifying it further using the characteristic time $\tau_{D,2} = \frac{\omega_2^2}{4D}$ we get:

$$G_D(\tau) = \frac{1/N_D \left[\frac{\sigma^2}{1+\frac{\tau}{\tau_{D,2}}} + \frac{1}{1+\sigma^2\frac{\tau}{\tau_{D,2}}} - \frac{4\sigma^2/(\sigma^2+1)}{1+2\frac{\tau}{\tau_{D,2}}/\left(1+\frac{1}{\sigma^2}\right)}\right]}{(\sigma^2-1)\sqrt{1+\frac{\tau}{S^2\tau_{D,0}}}} \qquad [3.13]$$

$S=z_0/\omega_0$ is the aspect ratio and $\sigma=\omega_2/\omega_1$ is the ratio of widths.

From Equation 3.13, three characteristics times can be extracted:

By definition, $\tau_{D,2} = \frac{\omega_2^2}{4D}$

$$\tau_{D,1} = \frac{\tau_{D,2}}{\sigma^2} = \frac{\omega_2^2}{4D}\frac{\omega_1^2}{\omega_2^2} = \frac{\omega_1^2}{4D}$$

$$\tau_{D,3} = \frac{\tau_{D,2}}{2}\left(1+\frac{1}{\sigma^2}\right) = \frac{\omega_2^2}{2*4D}\left(1+\frac{\omega_1^2}{\omega_2^2}\right) = \frac{(\omega_1^2+\omega_2^2)/2}{4D}$$

By substituting these times into equation 3.13 we get:

$$G_D(\tau) \approx \frac{1/N_D \left[\frac{\sigma^2}{1+\frac{\tau}{\tau_{D,2}}} + \frac{1}{1+\frac{\tau}{\tau_{D,1}}} - \frac{4\sigma^2/(\sigma^2+1)}{1+\frac{\tau}{\tau_{D,3}}}\right]}{(\sigma^2-1)\sqrt{1+\frac{\tau}{S^2\tau_{D,0}}}} \qquad [3.14]$$

In the case that σ~1, which is what we expect according to the results shown above, all of the three diffusion times are approximately the same and we can substitute $\tau_{D,2}$ for them in equation 3.14.

$$G_D(\tau) = \frac{1/N_D \left[\frac{\sigma^2}{1+\frac{\tau}{\tau_{D,2}}} + \frac{1}{1+\frac{\tau}{\tau_{D,2}}} - \frac{4\sigma^2/(\sigma^2+1)}{1+\frac{\tau}{\tau_{D,2}}} \right]}{(\sigma^2-1)\sqrt{1+\frac{\tau}{S^2\tau_{D,0}}}}$$

$$G_D(\tau) \approx \frac{1/N_D \frac{\sigma^2-1}{(\sigma^2+1)} \left[\frac{1}{1+\frac{\tau}{\tau_{D,2}}} \right]}{\left(\sqrt{1+\frac{\tau}{S^2\tau_{D,0}}} \right)} \qquad [3.15]$$

Since σ is a constant, Equation 3.15 now has the same form as the Gaussian ACF since $1/N_D \frac{\sigma^2-1}{(\sigma^2+1)}$ by definition is equal to $G_D(0)$. Figure 13 is a comparison of autocorrelation curves based on the model correlation functions for the Gaussian (Equation 2, Appendix A) and doughnut (Equation 3.10) focal profiles. The values for ω_0, ω_1 and ω_2 were obtained from the fits in Figure 10 as discussed above.

From observing the predicted autocorrelation functions for the Gaussian (solid line) and doughnut (dashed line) illumination profiles in Figure 13a, what immediately stands out is the difference in correlation amplitude where the doughnut amplitude is about three times smaller than that of the Gaussian

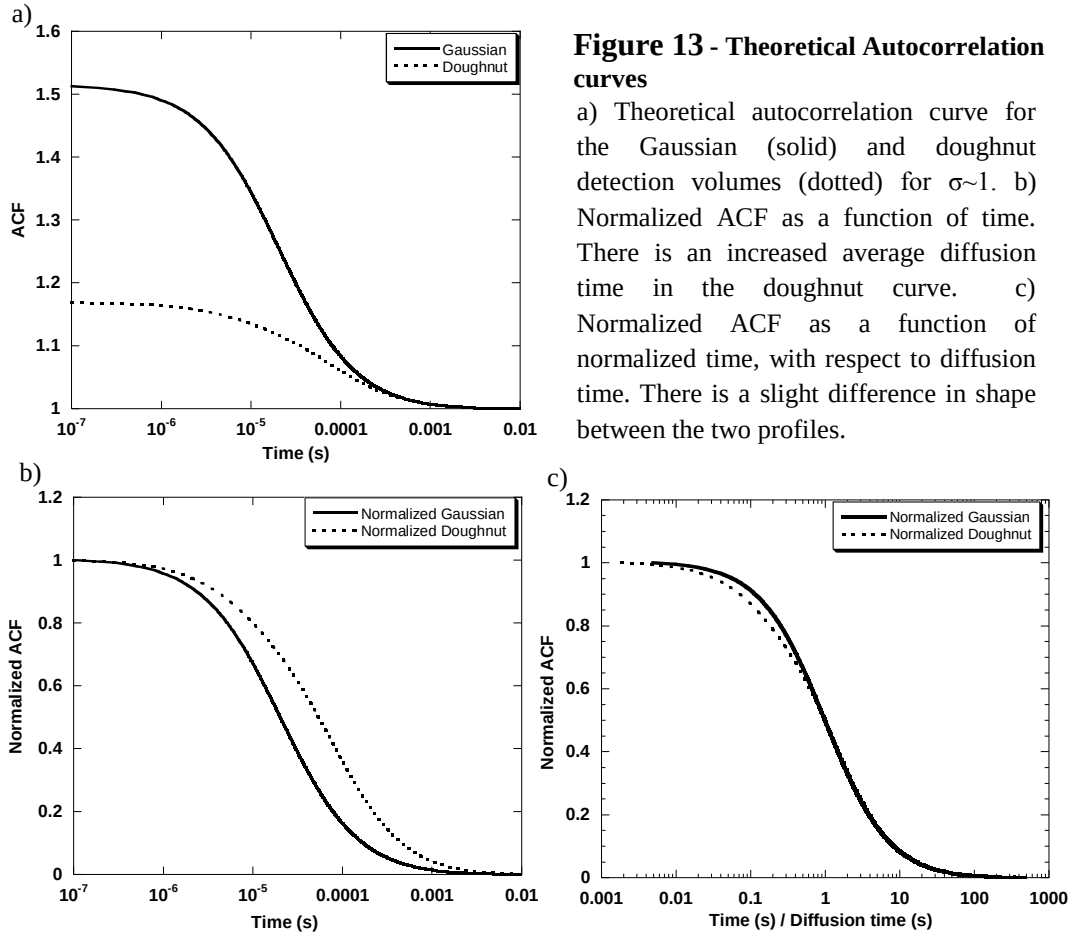

Figure 13 - Theoretical Autocorrelation curves

a) Theoretical autocorrelation curve for the Gaussian (solid) and doughnut detection volumes (dotted) for σ~1. b) Normalized ACF as a function of time. There is an increased average diffusion time in the doughnut curve. c) Normalized ACF as a function of normalized time, with respect to diffusion time. There is a slight difference in shape between the two profiles.

However in the doughnut case the amplitude does not directly give any information regarding the number of particles in the detection volume. The ratio of the CPPs can be calculated from:

$N_G = \langle C \rangle \pi^{3/2} \omega_0^2 z_0$ and $N_D = \pi^{3/2} z_0 \, [\omega_2^2 - \omega_1^2] \, \langle C \rangle$, giving:

$$\frac{CPP_D}{CPP_G} = \frac{\frac{I_D}{N_D}}{\frac{I_G}{N_G}} = \frac{N_G}{N_D} = \frac{[\omega_0^2]}{[\omega_2^2 - \omega_1^2]} \qquad [3.16]$$

Another quantity that can be a measure of the quality of the signal and corresponding autocorrelation function is the height of the autocorrelation function, $G_{G/D}(0)$ multiplied by the average intensity, $I_{G/D}*G_{G/D}(0)$. We call this the quality factor, Q and it can be calculated using $G_D(0) = \frac{1}{\langle C\rangle \pi^{3/2} z_0[\omega_2^2+\omega_1^2]}$ and $G_G(0) = \frac{1}{\langle C\rangle \pi^{3/2}\omega_0^2 z_0}$.

$$\frac{Q_D}{Q_G} = \frac{I_D/\langle C\rangle \pi^{3/2} z_0[\omega_2^2+\omega_1^2]}{I_G/\langle C\rangle \pi^{3/2}\omega_0^2 z_0} = \frac{\omega_0^2}{[\omega_2^2+\omega_1^2]} \qquad [3.17]$$

In the Gaussian case, $CPP_G = Q_G$ since the amplitude of the autocorrelation function is equal to $1/N_G$, but in the case of the doughnut, $CPP_D = \kappa Q_D$ where $\kappa = \frac{\sigma^2+1}{\sigma^2-1}$. The main reason for introducing the quality factor is that it is easier to measure the amplitude of the autocorrelation function precisely in the case of the doughnut as opposed to the value $1/N_D$ and since Q is proportional to CPP, the information it gives is analogous to that the CPP gives.

A more subtle effect highlighted in Figure 13a is the change in the transit times of fluorescent molecules through both detection volumes. Upon normalizing the curves in the y axis this effect becomes more clear and we can see that the average diffusion time for the doughnut is higher than that for the Gaussian. The larger diffusion time again is a consequence of the spreading of the PSF for the doughnut because it takes longer for the molecules to travel across the detection volume. In Figure 13c the horizontal axis which is time is also normalized with respect to the respective diffusion times for both detection volumes. Upon doing this the slight difference in the shape of both curves becomes

apparent and we know that the amplitude and average diffusion time are not the only parameters that set the two curves apart.

3.4.2 Experiments

In Figures 11 and 12 (Section 3.3), the measured intensity profiles of the Gaussian and doughnut were obtained and fit with a Gaussian and difference of Gaussians, respectively. From the fits, values of the widths, ω_0, ω_1 and ω_2 were then obtained. Just as measuring the ACF for a Gaussian PSF allows measuring ω_0 without having to visualize the profile, if the ACF calculation in the previous section is valid we should be able to obtain ω_2 and ω_1 from it in the case of the doughnut PSF. In order to do so we recorded autocorrelation curves at different confocal pinhole sizes for the dye Alexa Fluor 532 excited at 532 nm with and without the phase plate.

Figure 14,a-c shows representative autocorrelation curves taken with our home-built STED- FCS set-up. The blue curve and fit represent the Gaussian case and the red curve and fit represent the doughnut. Three different pinhole sizes of 50 µm, 75 µm, and 100 µm were used to remove out of focus signal. Equations 3.13 was used to fit the doughnut curves where the variables $G_D(0)$, N_D, $\tau_{D,2}$ and σ were varied and equation 3.9 was used to fit the Gaussian curves where the variables S, N_G and $\tau_{D,0}$ were varied.

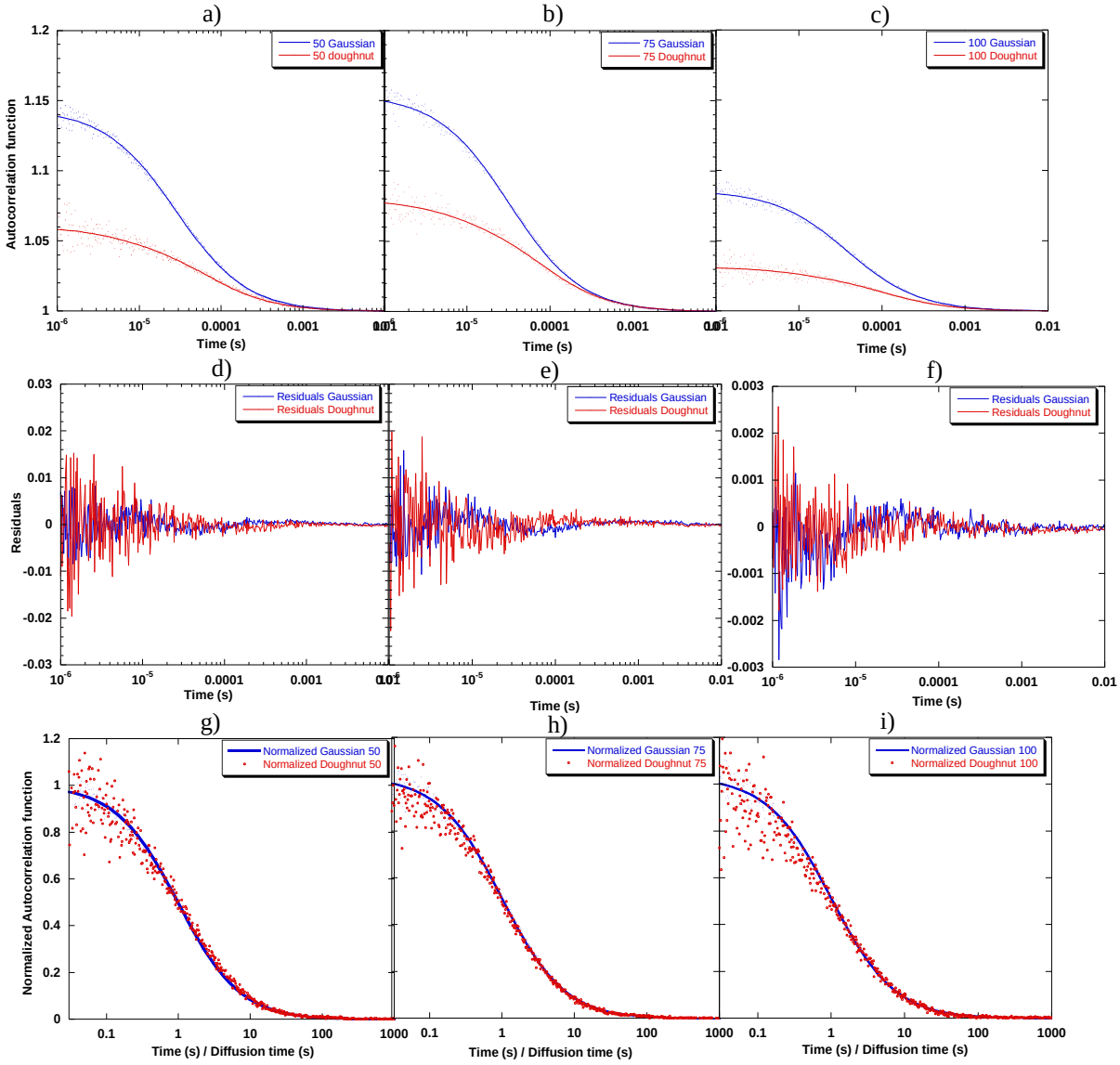

Figure 14 - Experimental autocorrelation curves

Autocorrelation as a function of lag time for pinhole sizes 50 µm (a, d, g), 75 µm (b, e, h) and 100 µm (c, f, i). Figures a-c show the original autocorrelation curves for the Gaussian (blue) and doughnut (red) for comparison along the same axis with fits. Figures d-f show the residuals for each fit and Figures g-i show the curves normalized in the vertical ($G(\tau)/G(0)$) and horizontal (τ/τ_D) axis. The blue curve represents the fit for the Gaussian.

The experimental curves in Figure 14 show similar trends as the theoretical curves of the Gaussian and doughnut autocorrelation functions in Figure 13. Some general trends that are visible without analysis are the decreased amplitude of the doughnut as compared to

the Gaussian and the increase in the average diffusion time for the doughnut. The purpose of figures 14 g-i was to look for a difference in shape between the doughnut and Gaussian curves by normalizing both axis, but unfortunately there is no substantial difference seen between the two for any pinhole size. The residuals for all the fits shown in Figure 14 d-f show that the fit is quite reasonable and only seems to get worse below 10 μs which is acceptable because the average diffusion time is longer than that. The doughnut curves were noisier than the Gaussian and therefore their residuals are larger. The summary of the results from the fits of the Gaussian are shown in Table 1 and that of the doughnut are shown in Table 2.

Pinhole (μm)	$G_G(0)$	N_G	S	I_G (kHz)	CPP_G, Q_G (kHz)	$\tau_{D,0,experimental}$ (s)
50	**0.1437±0.0002**	**6.95±0.01**	**8±1**	**222±2**	**31.9±0.3**	**(2.82±0.02)x10^{-}**
75	0.1543±0.0003	6.48±0.01	9±2	206±3	31.8±0.5	(3.24±0.03)x10^{-}
100	0.0857±0.0002	11.67±0.03	12±4	234±2	20.1±0.2	(3.79±0.05)x10^{-}

The parameters that were varied were S, NG and τD,0. The average intensity values, IG, were recorded during the experiment. The errors on the fit parameters were obtained from the least-square fit. The bold results indicate the optimal pinhole size for the Gaussian PSF due to the highest CPP, Q obtained.

Pinhole (μm)	$G_D(0)$	N_D	I_D (kHz)	Q_D (kHz)	CPP_D (kHz)	σ	$\tau_{D,2,experimental}$ (s)
50	0.0601±0.0004	0.65±150	128±2	7.7±0.2	196.9	1.04±4	(3±10)x10^{-5}
75	**0.0815±0.0004**	**0.65±70**	**115±2**	**9.4±0.2**	**176.9**	**1.05±2**	**(3±6)x10^{-5}**
100	0.0333±0.0002	0.74±80	154±2	5.1±0.1	208.1	1.04±4	(4±10)x10^{-5}

Table 2 - Doughnut parameters from Figure 14 obtained by fitting the doughnut curves with equation 3.13 [Fit 1].

The parameters that were varied were $G_D(0)$, N_D, $\tau_{D,2}$ and σ. The value of S was fixed at 8. The average intensity values, I_D, were recorded during the experiment. The errors shown were obtained from the least-square fit. The bold results indicate the optimal pinhole size for the doughnut PSF due to the highest Q obtained.

Table 1 shows the values of the variables obtained from fitting the Gaussian curves in Figure 14 a-c with equation 3.9. The CPP (which is the same as the quality factor, Q, in this case) decreases with increasing pinhole sizes indicating that for a Gaussian profile the optimal pinhole size range for removing out of focus signal is 50-75 μm. A trend is also seen in the average diffusion time which increases with increasing pinhole sizes which is expected since the increased width of the pinholes adds to the width of the effective PSF. The average number of particles is similar for the 50 and 75 μm case but definitely increases by a lot in the 100 μm case which corresponds to a wider PSF and is consistent with the larger diffusion time. An estimate of the value of $\tau_{D,0} = \omega_0^2/4D$, was calculated using the value of ω_0 obtained from the PSF shown in Figure 11 ($\omega 0 = 244.7$ nm) and the known diffusion coefficient for Alexa Fluor 546 ($D=341$ $\mu m^2/s$, Petrášek, Z. and Schwille, P., 2008) since D for the dye Alexa Fluor 532 was not available. The value for $\tau_{D,0}$ calculated was 3.7×10^{-5} s. This value is larger than the experimental values (Table 1), which means that ω_0 is smaller than what we measured for the image and/or that D is larger for Alexa 532 than it is for Alexa 546 (which is likely since Alexa 532 has a lower molecular weight than Alexa 546 (Alexa Fluor® Dye Selection Guide, 2005)). Hence, calibration of the set-up with a dye of known diffusion coefficient will be required in the future. As a side note, it is important to be cautious here to not think the ACF to exactly reflect the properties of the PSF since the effective PSF is modified by the presence of the pinhole and of eventual pinhole misalignment.

Table 2 shows the fit results in the doughnut case, where we again see a clear trend in the average diffusion time, which increases with increasing pinhole sizes. We would expect

the diffusion times to be higher for the doughnut than the Gaussian due to the spreading of the PSF. The theoretical average diffusion time ratio between the Gaussian and doughnut, $\tau_{D,2}/\tau_{D,0}$ is ~2.5 (Table 5). However, the extremely large error associated with the doughnut diffusion times makes it difficult to confirm this. The CPP for the 100 µm case is the highest with a value of 208.1 kHz. Surprisingly, the CPP for the 50 µm pinhole is higher than the 75 µm pinhole and a possible reason for this is that the 50 µm pinhole may be off-centre on the doughnut during this measurement and may be collecting intensity mainly from the doughnut ring which is brighter. This highlights the issue of proper pinhole alignment for the doughnut ACF. The Q values for all pinholes have very reasonable errors and since this value is the highest for the 75 µm pinhole case we can consider this to be the optimal pinhole size for the doughnut PSF. The errors on the CPP are too high for it to be a reliable guide in this case (not shown here but inferred from error on N_D). The values of σ for all three pinhole sizes are also comparable to the predicted value of 1.04 with an average value of ~1.04 but with a huge error associated with it. The only reliable parameter here with a small error is the quality factor.

Pinhole (µm)	$G_D(0)$	Q_D (kHz)	$\tau_{D,2,\ experimental}$ (s)
50	0.0576±0.0003	7.4±0.2	$5.2\pm0.1\times10^{-5}$
75	**0.0762±0.0003**	**8.8±0.2**	**$6.0\pm0.1\times10^{-5}$**
100	0.0301±0.0002	4.6±0.1	$8.0\pm0.3\times10^{-5}$

Table 3 - **Doughnut parameters from Figure 14 obtained by fitting with equation 3.15 [Fit 2] with the assumption, σ~1.**
The parameters that were varied were $G_D(0)$ and $\tau_{D,2.}$ S was fixed at 8.

Due to the unreliable nature of the fit with the exact ACF form, we decided to try a simpler fit of the doughnut using Equation 3.15, $G_D(\tau) = \frac{\sigma^2-1}{N_D(1+\sigma^2)\left(1+\frac{\tau}{\tau_{D,2}}\right)\left(\sqrt{1+\frac{\tau}{S^2\tau_{D,0}}}\right)}$,

which was derived with the assumption that σ~1. Based on the sigma values close to 1, obtained from the experimental PSF it is acceptable to use equation 3.15 to fit the doughnut curves in Figure 14 [Fit 2]. The two fit parameters were $\frac{1}{N_D}\frac{\sigma^2-1}{\sigma^2+1}$ and $\tau_{D,2}$ where the first parameter is equivalent to $G_D(0)$. This makes Equation 3.15 the same form as the Gaussian ACF. Table 3 shows the results obtained from the fit. The average diffusion times, $\tau_{D,2}$, increase with increasing pinhole sizes as expected. Also the $\tau_{D,2}$ values are much higher compared to the values obtained through fit 1 (Table 2) and the average ratio $\tau_{D,2}/\tau_{D,0}$ of ~1.9±0.1 (average from all pinholes) is close to the theoretical prediction (Table 5). In addition, the errors on the diffusion times are a magnitude smaller than what was obtained using the first fit. We cannot separate $G_D(0)$ into $1/N_D$ and σ, but we can calculate the quality factor (shown in Table 3) which is comparable to what was obtained using fit 1 (Table 2).

Table 4 is a comparison between the Gaussian and doughnut fits , while Table 5 shows the remaining predicted values. According to Table 5, the ratio $G_D(0)/G_G(0)$ should be equal to Q_D/Q_G, but that is not the case in the values obtained from the fits. The reason for this is that the prediction that they are equal is made with the assumption that the ratio I_D/I_G is 1, but I_D and I_G are different for each pinhole (Table 1 and 2) and that can account for the discrepancy between the two. On the other hand, Q_D/Q_G experimental and predicted are in good agreement with each other for fit 1 and fit 2 hence showing the

robustness of the Q factor as a standard parameter for measurement. Overall, upon comparing the two fits, fit 2 seems to be in better agreement with predicted values and gives a better estimate of the average diffusion times for each pinhole. Moreover the Q factor is an indispensible tool for testing the doughnut ACF due to the small error associated with its measurement and its rigidity in both fits.

Pinhole (μm)	$G_D(0)/G_G(0)$ [Fit 1]	**$G_D(0)/G_G(0)$ [Fit 2]**	Q_D/Q_G [Fit 1]	**Q_D/Q_G [Fit 2]**
50	0.418±0.003	**0.401±0.002**	0.241±0.008	**0.23±0.01**
75	0.528±0.004	**0.494±0.003**	0.29±0.01	**0.27±0.01**
100	0.388±0.003	**0.350±0.003**	0.253±0.007	**0.229±0.007**

Table 4 - Comparison between doughnut and Gaussian fits
Bold values indicate the better fit.

$G_D(0)/G$	Q_D/Q_G	$\tau_{D,1}/\tau_{D,0}$	$\tau_{D,2}/\tau_{D,0}$	$\tau_{D,3}/\tau_{D,0}$
0.24	0.24	2.4	2.6	2.5

Table 5 - Expected parameters
Expected values with ω_0=224.7 nm (Figure 11), ω_2 = 362.07 nm and ω_1 = 348.54 nm (Figure 12).

3.5 Quality factor

The ACF is very sensitive to changes in the detection volume shape and size (Ruttinger, S., et al., 2008). It could thus be a guide for assessing the quality of the doughnut and of that of the pinhole alignment. The doughnut correlation model described in the previous section could help conduct the alignment of a STED set-up in the same way that the Gaussian ACF is a reliable guide during alignment of an FCS set up (Enderlein, J., et al., 2004). We decided to test this theory further by using FCS to test for the presence of a central minimum in Q when the pinhole is perfectly aligned around the zero intensity region of the doughnut. The amplitude of the correlation particularly is very sensitive to

changes in the detection volume, hence we can also use the quality factor, Q to check for symmetry and overall quality of the doughnut.

3.5.1 Experimental method

The quality factor as shown earlier is proportional to the count per particle and we expect it to drop if a particle is in the low intensity region of the doughnut. Therefore we can use Q as a diagnostic tool to test for the presence of a central minimum in the doughnut profile. This experiment was performed with the dye Alexa Fluor 532 (Invitrogen, Life Technologies) at a concentration of 10nM. The power of the STED beam was kept constant at 25μW and several pinhole sizes, starting from 100 μm down to 25 μm were used.

For both illumination profiles, the procedure for this experiment was the same. After the pinhole was centrally positioned in x and y, it was translated along the y direction till the intensity count dropped to a relatively low value, indicating that most of the emission profile was being blocked. This can also be observed visually by planting a camera right after the pinhole and using a high concentration sample. The choice of the direction is arbitrary and as long as the illumination profile is isotropic it should not matter whether x or y is chosen as the direction of travel. After this, the pinhole was moved in equal increments towards the positive y direction till it reached the other extreme of the intensity profile. At each step the intensity history and correlation function were recorded for 120 seconds. The correlation functions were fit using MATLAB (program written by Amit Patel) and the quality factor was calculated for each position of the pinhole.

3.5.2 Q curves

Figure 15 shows all the quality factor curves as a function of pinhole position for pinhole sizes 100 µm, 50 µm and 25 µm.

Figure 15a (left panel) shows the normalized intensity for the Gaussian and doughnut detection volumes as a function of pinhole position. The doughnut intensity is about half of that of the Gaussian and both curves can be fitted with a Gaussian function. According to the fits, the width of the Gaussian is 63.2 µm and width of the doughnut is 82.9 µm which shows considerable increase in the doughnut case which is expected. However there is no indication of a central minimum in the intensity profile of the doughnut. Figure 15a (right panel) further shows the normalized quality factor as a function of the pinhole position. The ratio between the max Q value for the Gaussian and doughnut curves is higher compared to the intensity curves and close to 0.24 as expected. The doughnut profile is again broader with a width of 76.9 µm, while the Gaussian has a width of 48.2 µm. The Q curves for both cases are narrower than the intensity curves. Although this displays the credibility of the quality factor as an instrument for assessing the characteristics of the doughnut and helping with pinhole alignment, there is still no evidence of a central minimum. The reason is that since a 100 µm pinhole is much larger than the actual focal size for the doughnut profile it is too large to resolve the minima.

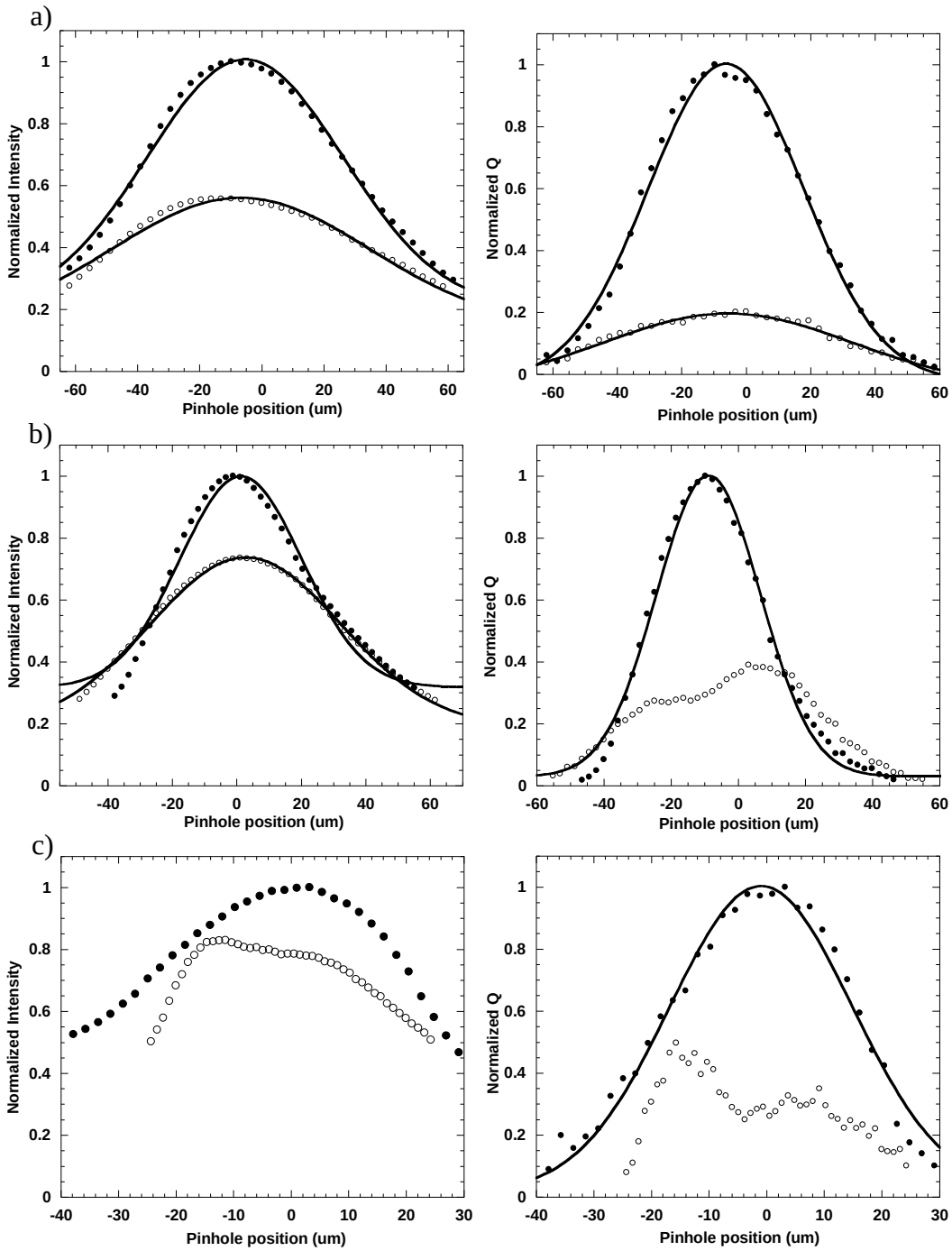

Figure 15 - Normalized Intensity and Normalized Q as a function of pinhole position.

Pinhole size a) 100 µm, b) 50 µm and c) 25 µm. Solid circles represent Gaussian curves and open circles represent doughnut curves.

According to the PSF of the doughnut obtained in Figure 12, the width of the doughnut hole is less than 200 nm in the focal plane since the size of the doughnut was slightly overestimated in this case. With an objective with 100X magnification, the size of the central minima should be less than 20 μm in the pinhole image plane.

Figure 15b (left panel) show the normalized intensity for the 50 μm pinhole and we can see that the width of both curves has decreased in comparison to the 100 μm pinhole. The Gaussian is now 37.8 μm and the doughnut is 59.0 μm. This is expected since the total width will roughly be the width of the PSF plus the width of the pinhole. The doughnut is still broader than the Gaussian which is expected but there is still only one central peak present. The amplitude of the doughnut is about 70% of the Gaussian which is counter intuitive since we would expect the difference in peak heights to be even greater for a smaller pinhole. Figure 15b (right panel) further shows the normalized quality factor as a function of pinhole size for the 50 μm pinhole and upon comparison with the intensity curve we see that the quality factor has been successful in finding a central minimum in the doughnut profile which was not evident in the former case. Even though it may not be that obvious due to the asymmetry of the doughnut, there are two peaks present. Finally in order to test the validity of the quality factor even further one more pinhole size was tested. Figure 15c shows the normalized intensity and quality factor for the 25 μm pinhole. Due to the extremely small size of this pinhole, the correlation curves were quite noisy but in spite of this details such as the flattening of the intensity at the top with a slight decrease in the centre were captured. In the normalized Q curve, a clear dip in the middle with two peaks on either side can be seen, even though the doughnut is still not

completely symmetric which probably reflects the imperfect quality of the doughnut formed with the present phase plate. What is great about combining the quality factor with a pinhole size this small is its ability to identify even a slight peak such as the one on the right in Figure 15c. Upon converting to the size of the profile in the focal plane by dividing by the magnification of the objective lens, it is interesting to note here that the width of the doughnut is approximately 450 nm and the width of the Gaussian is approximately 250 nm which seems reasonable. Overall the quality factor has been extremely effective in identifying and expressing the characteristics of the doughnut detection volume that were not evident in the intensity profile. When combined with a small pinhole size that is still large enough to get a clear correlation signal it can be a great evaluation tool for the presence of a doughnut, symmetric or otherwise. For alignment purposes as well, having a minimum in Q is great because we can look for this minimum for perfect alignment of the beam to the pinhole.

3.6 Road map for alignment of STED and excitation beams for STED-FCS

In order for STED to be effective, complete alignment of the STED and excitation focal spots has to occur in the lateral and axial planes. So far efforts were being made to align the beams visually on a camera or by using the photon count as a guide. If the phase plate is removed from the STED beam path then we expect the STED beam to completely deplete fluorescence from the sample upon super-position with the excitation beam. After superposition of both beams this was tested with a sample containing the dye ATTO 425 and there was hardly any reduction in the photon count. We attributed this to a low STED

intensity and hence raised the intensity to almost 5 times the original value. This also did not make a difference and so we came to the conclusion that the alignment of the two beams seems to be the issue here. Due to longitudinal chromatic aberrations introduced by the collimation and objective lens, there always seems to be an offset in the axial plane in the PSF's for different wavelengths between 90-115 nm. Since the PSF's are quite extended in the z direction (about 1000 nm), this offset should not affect STED measurements to a great extent (Wildanger, D. et al., 2009). However the collimation should also be checked for both beams to ensure that it does not give rise to even further misalignment in the z direction.

The methods so far used to align in the lateral plane tend to have a higher degree of error associated with them and hence a new plan for alignment of the two beams has been devised, which will be part of the future plans for this project. This will be a follow-up study to show the effectiveness of FCS as an aligning agent. Introduced by Petra Schwille in 1997, the cross correlation can be used to show complete super position of two focused beams. A cross correlation function between two channels basically represents the correlation coefficient between two fluorescent signals in time. If a fluorescent dye has the ability to fluoresce at two different excitation wavelengths, 442 nm and 532 nm specifically, then the cross correlation function can be used to determine whether there is complete overlap of the two foci. For the purposes of the alignment, both lasers will have Gaussian illumination profiles at first but then one could develop the theoretical background to check what the correlation coefficient would be between a Gaussian and a doughnut beam. The experimental set-up would include separation of the emission after

the pinhole using a beam expander followed by appropriate emission filters. The detection would then occur with two different detectors and the cross correlation would be calculated using a hardware correlator. A cross correlation experiment tends to give 3 curves; 2 autocorrelation curves for each channel and one combined cross correlation curve. Generally, due to the wave nature of light, different wavelengths tend to have different sized focal spots (equation 1.1). If the smaller focal spot is completely within the larger focal spot then the amplitude of the correlation curve for the smaller channel should be equivalent to the cross correlation curve (Schwille, P. et al., 1997). Any deviation from this would indicate partial overlap of the two observation volumes. One of the drawbacks to this technique is that dyes with two excitation maxima specifically at 442 nm and 532 nm are not readily available commercially. A possible way to produce such a combination would be to fluorescently label vesicles with both dyes. Nevertheless, this is a great quantitative tool for alignment of the two beams in the lateral plane and we hope that it will prove effective in completing the final step of the STED-FCS project.

CONCLUSION

In this report, we discussed super-resolution microscopy in the biological sciences, particularly the principle behind STED microscopy and the success of this technique especially in imaging live cells below the Abbe Limit. The dynamic duo of STED-FCS has proved to be very effective in classifying diffusive behaviour as simple or anomalous specially in membrane systems. The motivation behind STED-FCS for us in particular

was to continue the study of diffusion in crowded media using variable length scale-FCS since anomalous behaviour implies a length scale dependent diffusion coefficient. Therefore to witness an anomalous diffusion power law which we suspect is seen only at sub-diffraction length scales we need to perform FCS experiments at the length scales afforded by STED. With this in mind, we set out to build a custom STED-FCS microscope. Since obtaining a symmetric doughnut can be difficult due to the amount of precise alignment required we decided to tackle this problem using FCS as a guide. Since we already know from literature that the PSF of a regular excitation spot can be approximated using a Gaussian function, we decided to exploit this idea and define the PSF for a doughnut excitation spot as a difference of two Gaussian functions. The ratio of the widths of the two Gaussians we obtained after fitting the PSF for an imaged doughnut was 1.04 comparable to the theoretical prediction of 1.03. We then calculated the autocorrelation function using this idea and fit experimental curves with this function to see the validity of our model. In the Gaussian case, the count per particle (CPP) obtained from the ACF is a very effective guide used during alignment. Therefore we did the same for the doughnut, but introduced a new quantity called the quality factor, Q, which is proportional to the CPP but easier to obtain. The quality factor was successful in showing characteristics of the doughnut, like the a central minimum intensity point not evident from looking at just the intensity profile especially at smaller pinhole sizes of about 25 μm. Hence, the quality factor can be a very helpful tool in precise alignment of the pinhole and in obtaining a symmetric doughnut for an effective STED-FCS experiment. Lastly, we outlined a road map for alignment of the excitation and STED beams in the

lateral plane using the cross correlation function as a guide. We already knew that FCS is a very powerful technique capable of extracting information such as diffusion times, concentrations, anomalous exponents etc. but this study has further highlighted the ability of the autocorrelation function to be used as a very effective alignment tool as well.

REFERENCES

ATTO 425/ Spectra_XLS, ATTO-TEC GmbH. Retrieved on Dec 15, 2012. < https://www.atto-tec.com/index.php?id=113&no_cache=1&L=1>

Alexa Fluor® Dye Selection Guide. (2005). Retrieved Jan 1, 2013, from Invitrogen web site: www.invitrogen.com/.../O-063190-Alexa-Fluor-SelectionGuide.pdf

Banks, S. and Fradin, C. (2005). Anomalous diffusion of proteins due to molecular crowding. *Biophysical Journal*, 89, 2960-71.

Bates, M., Huang, B., Dempsey, G.T., Zhuang, X.W. (2007). Multicolour super-resolution imaging with photo-switchable fluorescent probes. *Science*, 317, 1749-53.

Betzig, E., Patterson, G.H., Sougrat, R., Lindwasser, O.W., Olenych, S., Bonifacino, J.S., Davidson, M.W., Lippincott-Schwartz, J., Hess, H.F. (2006). Imaging Intracellular fluorescent proteins at nanometer resolution. *Science*, 313, 1642-45.

Cole. R.W., Jinadasa, T. and Brown, C.M. (2011). Measuring and interpreting point spread functions to determine confocal microscope resolution and ensure quality control. *Nature Protocols*, 6(12), 1929-41.

D480/30m, Chroma Technology Corp. Retrieved on Dec 15, 2012. < http://www.chroma.com/product/individual-filters-mirrors/widefield-microscopy/D480_x_30m-EM>

Daniel Banks, "Fluorescence correlation spectroscopy studies characterizing diffusion and photophysical properties of proteins" (January 1, 2008). *ETD Collection for McMaster University.* Paper AAINR57801. http://digitalcommons.mcmaster.ca/dissertations/AAINR57801

Diaspro, A. (2010). *Nanoscopy and Multidimensional Optical Fluorescence Microscopy*. Chapman and Hall/CRC.

Donnert, G., Keller, J., Medda, R., Andrei, M., Rizzoli, S., Luhrmann, R., Jahn, R., Eggeling, C., Hell, S. (2006). Macromolecular-scale resolution in biological fluorescence microscopy. *Proceedings of the National Academy of Sciences of the United States of America*, 103(31), 11440-45.

Dyba, M., Jakobs, L., Hell, S.W. (2003). Immunofluorescence stimulated emission depletion microscopy. *Nature Biotechnology*, 21, 1303-04.

Eggeling, C., Ringermann, C., Medda, R., Schwarzmann, G., Sandhoff, K., Polyakova, S., Belov, V., Hein, B., Middendorff, C., Schönle, A. and Hell, S.W. (2009). Direct

observation of the nanoscale dynamics of membrane lipids in a living cell. *Nature*, 457, 1159-62.

Enderlein, J., Gregor, I., Patra, D. and Fitter, J. (2004). Art and Artefacts of Fluorescence Correlation Spectroscopy. *Current Pharmaceutical Biotechnology*, 5, 155-61.

Fatin-Rouge, N., Starchev, K. and Buffle, J. (2004). Size Effects on Diffusion Processes within Agarose Gels. *Biophysical Journal*, 86(5), 2710-19.

fluorescent molecules by FCS: Impact for immunobiology. *Proceedings of the National Academy of Sciences of the United States of America*, 98(20), 11509-14.

Földes-Papp, Z., Demel, U., Tilz, G.P. (2001). Ultrasensitive detection and identification of

Gugel, H., Bewersdorf, J., Jakobs, S., Engelhardt, J., Storz, R., Hell, S.W. (2004). Cooperative 4Pi excitation and detection yields sevenfold sharper optical sections in live-cell microscopy. *Biophysical Journal*, 87, 4146-52.

Gustafsson, M. G. L. (2000). Surpassing the lateral resolution limit by a factor of two using structured illumination microscopy. *Journal of Microscopy*, 198, 82-87.

Hein, B., Willig, K.I., Hell, S.W. (2008). Stimulated emission depletion (STED) nanoscopy of a fluorescent protein-labeled organelle inside a living cell. *Proceedings of the National Academy of Science, U.S.A.*, 105, 14271-76.

Hell, S.W. & Kroug, M. (1995). Ground-state-depletion fluorescence microscopy: a concept for breaking the diffraction resolution limit. *Applied Physics B: Lasers and Optics*, 60(5), 495–97.

Hell, S.W. & Stelzer, E.H.K. (1992). Fundamental improvement of resolution with a 4Pi-confocal microscope using two-photon excitation. *Optics Communications*, 93, 277-82.

Hell, S.W. & Wichmann, J. (1994). Breaking the diffraction resolution limit by stimulated emission: stimulated-emission-depletion fluorescence microscopy. *Optics Letters*, 19(11), 780-82.

Hess, S.T. and Webb, W.W. (2002). Focal Volume Optics and Experimental Artifacts in Confocal Fluorescence Correlation Spectroscopy. *Biophysical Journal*, 83(4), 2300-17.

Juette, M.F., Gould, T.J., Lessard, M.D., Mlodzianoski, M.J., Nagpue, B.S., Bennett, B.T., Hess, S.T., Bewersdorf, J. (2008). Three-dimensional sub-100 nm resolution fluorescence microscopy of thick samples. *Nature Methods*, 5, 527-29.

Kastrup L., Blom H., Eggeling C. and Hell S.W. (2005). Fluorescence fluctuation spectroscopy in subdiffraction focal volumes. *Physical Review Letters*, 94(17), 178104-1:4.

Koppel, D. (1974). Statistical accuracy in fluorescence correlation spectroscopy. *Physical Review Letters: A*, 10(6), 1938-45.

Max Plank Institute for Biophysical Chemistry. (2012). Stimulated Emission Depletion (STED). Retrieved from <http://www.nanobiophotonics.mpibpc.mpg.de/research/methods/STED.html>

Moneron, G., Medda, R., Hein, B., Giske, A., Westphal, V., Hell, S.W. (2010). Fast STED microscopy with continuous wave fiber lasers. *Optics Express*, 18(2), 1302-09.

NC191968 - z442rdc, Chroma Technology Corp. Retrieved on Dec 15, 2012. < http://www.chroma.com/product/custom-and-clearance/custom-inventory/dichroic-NC191968>

NC282471 - z442/532/633rpc, Chroma Technology Corp. Retrieved on Dec 15, 2012. < http://www.chroma.com/product/custom-and-clearance/custom-inventory/dichroic-NC282471>

Petrášek, Z. and Schwille, P. (2008). Precise Measurement of Diffusion Coefficients using Scanning Fluorescence Correlation Spectroscopy. *Biophysical Journal*, 94(4), 1437-48.

Rankin, B.R., Kellner, R.R. and Hell, S.W. (2008). Stimulated-emission-depletion microscopy with a multicolor stimulated-Raman-scattering light source. *Optics Letters*, 33(21), 2491-93.

Ries, J. & Schwille, P. (2008). New concepts for fluorescence correlation spectroscopy on membranes. *The Journal of Physical Chemistry*, 10(24), 3487-97.

Rust, M.J., Bates, M., Zhuang, X.W. (2006). Sub-diffraction-limit imaging by stochastic optical reconstruction microscopy (STORM). *Nature Methods*, 3, 793-95.

Rüttinger, S., Buschmann, V., Krämer, B., Erdmann, R., Macdonald, R. and Koberling, F. (2008). Comparison and accuracy of methods to determine the confocal volume for quantitative fluorescence correlation spectroscopy. *Journal of Microscopy*, 232(2), 343-52.

Schwille, P., Meyer-Almes, F. and Rigler, R. (1997). Dual-Color Fluorescence Cross-Correlation Spectroscopy for Multicomponent Diffusional Analysis in Solution. *Biophysical Journal*, 72, 1878-86.

Tian, B. and Pu, J. (2011). Tight focusing of a double-ring-shaped, azimuthally polarized beam. *Optics Letters*, 36(11), 2014-16.

Weiss, M., Elsner, M., Kartberg, F., Nilsson, T. (2004). Anomalous Subdiffusion Is a Measure for Cytoplasmic Crowding in Living Cells. *Biophysical Journal*, 87(5), 3518-24.

Widengren, J., Rigler, R. and Mets, U. (1994). Triplet-state monitoring by fluorescence correlation spectroscopy. *Journal of Fluorescence*, 4(3), 255-58.

Wildander, D., Bückers, J., Westphal, V., Hell, S. and Kastrup, L. (2009). A STED microscope aligned by design. *Optics Express*, 17(18), 16100-10.

Willig, K., Harke, B., Medda, R. and Hell, S. (2007). STED microscopy with continuous wave beams. *Nature Methods*, 4(11), 915-18.

Zhang, B., J. Zerubia, J.C. Olivo-Marin. (2007). Gaussian approximations of fluorescence microscope point-spread function models. *Applied Optics*, 46, 1819–29.

APPENDIX A - Calculation of the Autocorrelation Function for a Gaussian Illumination Profile

The autocorrelation function describes the self-similarity of a signal in time. With lag time, τ, and the fluorescence signal as a function of time, F(t) we can define the correlation between the fluorescence signal as (Foldes-Papp, Z et. al, 2001):

$$G(\tau) = \frac{\langle F(t+\tau)F(t)\rangle}{\langle F(t)\rangle^2}$$

The fluctuations of the fluorescence signal, δF(t), are the deviations from the average fluorescence signal and are written as

$$\delta F(t) = F(t) - \langle F\rangle$$

Thus the correlation function becomes

$$G(\tau) = \frac{\langle \delta F(t+\tau)\delta F(t)\rangle}{\langle F(t)\rangle^2} + 1$$

The fluorescence signal and the fluctuation over space $\vec{r} = (x, y, z)$ for a confocal set up can be written as

$$F(t) = \kappa \int I(\vec{r}).CEF(\vec{r}).C(\vec{r},t)d\vec{r}$$

$$\delta F(t) = \kappa \int I(\vec{r}).CEF(\vec{r})\delta C(\vec{r},t)d\vec{r}$$

Here κ is a factor that depends on the quantum yield of the fluorophore, collection efficiency of the instrument and the fluorophore absorption cross section. $I(\vec{r})$ is simply the illumination intensity profile and $C(\vec{r})$ gives the concentration of the sample. $CEF(\vec{r})$ is the normalized collection efficiency function of the system and depends on the transmission property of the pinhole and the point spread function (PSF) of the beam.

By inserting the above functions into the correlation function we get

$$G(\tau) = \frac{\int\int I(\vec{r})I(\vec{r}').CEF(\vec{r}).CEF(\vec{r}').\langle\delta C(\vec{r}', t+\tau)\delta C(\vec{r}, t)\rangle d\vec{r}d\vec{r}'}{\langle C\rangle^2(\int I(\vec{r}).CEF(\vec{r})d\vec{r})^2} + 1$$

The last term in the numerator which is the correlation of concentration fluctuations can be described by the diffusion propagator since the fluorophores are diffusing.

The above expression can now be written as

$$G(\tau) = \frac{\int\int W(\vec{r})W(\vec{r}').\langle C\rangle e^{\frac{-(r-r')^2/4D\tau}{8(\pi D\tau)^{3/2}}} d\vec{r}d\vec{r}'}{\langle C\rangle^2(\int W(\vec{r})d\vec{r})^2} + 1 \qquad (1)$$

where $W(\vec{r}) = I(\vec{r}).CEF(\vec{r})$

Equation 1 is the general form for a correlation function and depending on the type of PSF the function can be integrated and a solution can be obtained. Since confocal microscopy uses a Gaussian illumination profile with $W(\vec{r}) = e^{\frac{-2x^2}{w_o^2}} e^{\frac{-2y^2}{w_o^2}} e^{\frac{-2z^2}{z_o^2}}$, we can insert it into equation 1 and integrate.

Solution of correlation function for a Gaussian profile

$$G_G(\tau) = \frac{\left(\int\int e^{\frac{-2x^2}{w_o^2}} e^{\frac{-2x'^2}{w_o^2}} e^{\frac{-(x-x')^2}{4D\tau}}\right)\left(\int\int e^{\frac{-2y^2}{w_o^2}} e^{\frac{-2y'^2}{w_o^2}} e^{\frac{-(y-y')^2}{4D\tau}}\right)\left(\int\int e^{\frac{-2z^2}{z_o^2}} e^{\frac{-2z'^2}{z_o^2}} e^{\frac{-(z-z')^2}{4D\tau}}\right) dxdx'dydy'dzdz'}{\langle C\rangle 8(\pi D\tau)^{3/2}\left(\int e^{\frac{-2x^2}{w_o^2}} e^{\frac{-2y^2}{w_o^2}} e^{\frac{-2z^2}{z_o^2}} dxdydz\right)^2}$$

$$+ 1$$

By using the basic Gaussian integral solution for the regular terms

$$\int_{-\infty}^{\infty} dx e^{-ax^2} = \sqrt{\frac{\pi}{a}}$$

and by completing the square for the cross terms and using the resultant expression

$$\int_{-\infty}^{\infty} dx e^{-ax^2+bx} = \int_{-\infty}^{\infty} dx e^{-a(x-\frac{b}{2a})^2+\frac{b^2}{4a}} = \sqrt{\frac{\pi}{a}} e^{\frac{b^2}{4a}}$$

we get the result

$$G_G(\tau) = \frac{1}{\langle C\rangle \pi^{3/2} w_o^2 z_o} \left(1+\frac{4D\tau}{w_o^2}\right)^{-1} \left(1+\frac{4D\tau}{z_o^2}\right)^{-1/2} + 1 \quad (2)$$

The quantity $G_G(0) = 1/(\langle C\rangle \pi^{3/2} w_o^2 z_o)$ is a constant and is estimated by the amplitude of the correlation function.

The Gaussian volume can be calculated using

$$V_G = \iiint e^{\frac{-2x^2}{\omega_0^2}} e^{\frac{-2y^2}{\omega_0^2}} e^{\frac{-2z^2}{z_0^2}} dxdydz$$

$$= \pi^{3/2} \omega_0^2 z_0$$

The number of particles in the Gaussian volume can be given by $N_G = \langle C\rangle \pi^{3/2} \omega_0^2 z_0 = \frac{1}{G(0)}$. Using the expression $D = \frac{w_o^2}{4\tau_{D,0}}$, we can simplify equation 2 to:

$$G(\tau) = \frac{1/N_G}{\left(1+\left(\frac{\tau}{\tau_{D,0}}\right)\right)\left(1+\frac{1}{S^2}\frac{\tau}{\tau_{D,0}}\right)^{1/2}}$$

(3)

Here, $S^2 = \frac{z_o^2}{w_o^2}$, is the aspect ratio.

APPENDIX B - Calculation of the Autocorrelation Function for the Doughnut Illumination Profile

The PSF for the doughnut illumination profile will be defined as a difference of Gaussian functions as shown below.

$$I_D(x,y,z) = \left[e^{\frac{-2x^2}{\omega_2^2}} e^{\frac{-2y^2}{\omega_2^2}} - e^{\frac{-2x^2}{\omega_1^2}} e^{\frac{-2y^2}{\omega_1^2}} \right] e^{\frac{-2z^2}{z_0^2}}$$

The general autocorrelation equation shown in Appendix A is:

$$G(\tau) = \frac{\int\int W(\vec{r})W(\vec{r}\,').\langle C\rangle e^{\frac{-(r-r')^2/4D\tau}{8(\pi D\tau)^{3/2}}} d\vec{r}d\vec{r}\,'}{\langle C\rangle^2 (\int W(\vec{r})d\vec{r})^2} + 1$$

Inserting $I_D(x,y,z)$ as W(r) and $I_D(x',y',z')$ as W(r') into the numerator (num) gives:

$$G_D(\tau)(num) = \frac{1}{8(\pi D\tau)^{3/2}} \iiint \left(e^{\frac{-2x^2}{\omega_2^2}} e^{\frac{-2y^2}{\omega_2^2}} e^{\frac{-2z^2}{z_0^2}} - e^{\frac{-2x^2}{\omega_1^2}} e^{\frac{-2y^2}{\omega_1^2}} e^{\frac{-2z^2}{z_0^2}} \right) \left(e^{\frac{-2x'^2}{\omega_2^2}} e^{\frac{-2y'^2}{\omega_2^2}} e^{\frac{-2z'^2}{z_0^2}} - e^{\frac{-2x'^2}{\omega_1^2}} e^{\frac{-2y'^2}{\omega_1^2}} e^{\frac{-2z'^2}{z_0^2}} \right) \left(e^{\frac{-(x-x')^2}{4D\tau}} e^{\frac{-(y-y')^2}{4D\tau}} e^{\frac{-(z-z')^2}{4D\tau}} \right) dx dx' dy dy' dz dz'$$

Multiplying the above terms out with each other:

(on next page)

$$G_D(\tau)(num)$$

$$= \frac{1}{8(\pi D\tau)^{3/2}} \iiint \left(e^{\frac{-2x^2}{\omega_2^2}} e^{\frac{-2y^2}{\omega_2^2}} e^{\frac{-2z^2}{z_0^2}} \right) \left(e^{\frac{-2x\prime^2}{\omega_2^2}} e^{\frac{-2y\prime^2}{\omega_2^2}} e^{\frac{-2z\prime^2}{z_0^2}} \right) \left(e^{\frac{-(x-x')^2}{4D\tau}} e^{\frac{-(y-y')^2}{4D\tau}} e^{\frac{-(z-z')^2}{4D\tau}} \right)$$

$$- \left(e^{\frac{-2x^2}{\omega_2^2}} e^{\frac{-2y^2}{\omega_2^2}} e^{\frac{-2z^2}{z_0^2}} \right) \left(e^{\frac{-2x\prime^2}{\omega_1^2}} e^{\frac{-2y\prime^2}{\omega_1^2}} e^{\frac{-2z\prime^2}{z_0^2}} \right) \left(e^{\frac{-(x-x')^2}{4D\tau}} e^{\frac{-(y-y')^2}{4D\tau}} e^{\frac{-(z-z')^2}{4D\tau}} \right)$$

$$- \left(e^{\frac{-2x^2}{\omega_1^2}} e^{\frac{-2y^2}{\omega_1^2}} e^{\frac{-2z^2}{z_0^2}} \right) \left(e^{\frac{-2x\prime^2}{\omega_2^2}} e^{\frac{-2y\prime^2}{\omega_2^2}} e^{\frac{-2z\prime^2}{z_0^2}} \right) \left(e^{\frac{-(x-x')^2}{4D\tau}} e^{\frac{-(y-y')^2}{4D\tau}} e^{\frac{-(z-z')^2}{4D\tau}} \right)$$

$$+ \left(e^{\frac{-2x^2}{\omega_1^2}} e^{\frac{-2y^2}{\omega_1^2}} e^{\frac{-2z^2}{z_0^2}} \right) \left(e^{\frac{-2x\prime^2}{\omega_1^2}} e^{\frac{-2y\prime^2}{\omega_1^2}} e^{\frac{-2z\prime^2}{z_0^2}} \right) \left(e^{\frac{-(x-x')^2}{4D\tau}} e^{\frac{-(y-y')^2}{4D\tau}} e^{\frac{-(z-z')^2}{4D\tau}} \right) dxdx'dydy'dzdx'$$

The above four expressions can be integrated separately to arrive at the solution for the numerator (not shown here).

For the denominator of the autocorrelation equation we have:

$$G_D(\tau)(den) = \langle C \rangle^2 \iiint \left(e^{\frac{-2x^2}{\omega_2^2}} e^{\frac{-2y^2}{\omega_2^2}} e^{\frac{-2z^2}{z_0^2}} - e^{\frac{-2x^2}{\omega_1^2}} e^{\frac{-2y^2}{\omega_1^2}} e^{\frac{-2z^2}{z_0^2}} \right)^2 dxdydz$$

By solving for $G_D(\tau)$ (num) and $G_D(\tau)$ (den) and then combining the two we get:

$$G_D(\tau) = \frac{\frac{\omega_2^2}{\frac{4D\tau}{\omega_2^2} + 1} + \frac{\omega_1^2}{\frac{4D\tau}{\omega_1^2} + 1} - \frac{4\omega_2^2\omega_1^2}{8D\tau + \omega_2^2 + \omega_1^2}}{\langle C \rangle \pi^{3/2} z_0 \left[\omega_2^2 - \omega_1^2\right]^2 \sqrt{\frac{4D\tau}{z_0^2} + 1}}$$

APPENDIX C - TABLE OF DYES USED IN STED MICROSCOPY

Dye (Manufacturer)	Exc. λ	Exc. pulse length	STED λ	STED pulse length	Avg. STED Power	Spatial resolution (direction)	Reference
ATTO 425 (ATTO-TEC GmbH)	440 nm	130 ps	532 nm	1 ns	24-162 μW	70-80 nm (xy)	B. Rankin et al., Opt. Lett. 33, 2491 (2008)
Mn doped ZnSe Quantum dots	440 nm	< 90 ps	676 nm	cw	-	45 nm (xy)	S.Irvine et al., Angew. Chem. Int. Ed. 47, 2685 (2008)
ATTO 532 (ATTO-TEC GmbH)	470 nm	100 ps	615 nm	200 ps	14-18 mW	66-72 nm (xy)	K. Willig et al., Nature 440, 935 (2006) J. Sieber et al., Biophys. J. 90, 2843 (2006) K. Willig et al., New J. Phys. 8, 106 (2006)
ATTO 532 (ATTO-TEC GmbH)	470 nm	80 ps	603 nm	280 ps	0.5 mW	< 25 nm (xy)	G. Donnert et al., Proc. Natl. Acad. Sci. USA 103, 11440 (2006)
Alexa Fluor 488 (Invitrogen Corp.)	488 nm	cw	592 nm	cw	< 600 mW	< 60 nm (xy)	G. Moneron et al., Opt. Expr. 18, 1302 (2010)
Chromeo 488 (Actif Motif Inc.)	488 nm	cw	592 nm	cw	< 600 mW	< 60 nm (xy)	G. Moneron et al., Opt. Expr. 18, 1302 (2010)
Oregon Green 488 (Invitrogen Corp.)	488 nm	cw	592 nm	cw	< 600 mW	< 60 nm (xy)	G. Moneron et al., Opt. Expr. 18, 1302 (2010)
FITC	488 nm	cw	592 nm	cw	< 600 mW	< 60 nm (xy)	G. Moneron et al., Opt. Expr. 18, 1302 (2010)
DY-495	488 nm	cw	592 nm	cw	< 600 mW	< 60 nm (xy)	G. Moneron et al., Opt. Expr. 18, 1302 (2010)
Citrine	488 nm	cw	592 nm	cw	112 mW	~ 60 nm (xy)	B. Hein et al., Proc. Natl. Acad. Sci. USA 105, 14271 (2008)
ATTO 532 (ATTO-TEC GmbH)	488 nm	120 ps	600 nm	200 ps	-	< 40 nm (xy)	L. Meyer et al., Small 4, 1095 (2008)
Chromeo 488 (Actif Motif Inc.)	488 nm	140 ps	602 nm	200 ps	0.6 mW	~ 30 nm (xy)	L. Meyer et al., Small 4, 1095 (2008) (Supporting Material)
ATTO 532 (ATTO-TEC GmbH)	488 nm	100 ps	615 nm	200 ps	16 mW	60-70 nm (xy)	D. Fitzner et al., EMBO J. 25, 5037 (2006); R. Kellner, Neurosci. 144, 135 (2007)
DY-485XL (Dynomics GmbH)	488 nm	<100 ps	647 nm	~ 200 ps	(20+3) mW	40-45 nm (xyz)	R. Schmidt et al., Nat. Meth. 5, 539 (2008)
GFP	490 nm	100 ps	575 nm	200 ps	7.2 mW	~ 70 nm (xy)	K. Willig et al., Nat. Meth. 3, 721 (2006)

Citrine	490 nm	100 ps	598 nm	300 ps	36 mW	48 nm (xy)	B. Hein et al., Proc. Natl. Acad. Sci. USA 105, 14271 (2008)
YFP	490 nm	100 ps	598 nm	300 ps	18 mW	~70 nm (xy)	U. V. Nägerl et al., Proc. Natl. Acad. Sci. USA 105, 18982 (2008)
ATTO 565 (ATTO-TEC GmbH)	532 nm	~ 90 ps	640 nm	~90 ps	-	30-40 nm (xy)	D. Wildanger et al., Opt. Expr. 16, 9614 (2008)
Sulfonated & rigidized rhodamine derivatives	532 nm	100 ps	640 nm	~300 ps	-	< 90 nm (xy)	V. Boyarskiy et al., Chem. Eur. J. 14, 1784 (2008)
ATTO 565 (ATTO-TEC GmbH)	532 nm	cw	647 nm	cw	114 mW	~ 60 nm (xy)	K. Willig et al., Nat. Meth. 4, 915 (2007)
NK51 (ATTO-TEC GmbH)	532 nm	< 100 ps	647 nm	~ 200 ps	(20+3) mW	40-45 nm (xyz)	R. Schmidt et al., Nat. Meth. 5, 539 (2008)
Nitrogen vacancies in diamond	532 nm	60 ps	775 nm	3.2 ns	850 mW	6 nm (xy)	Rittweger et al., Nat. Photon. 3, 144 (2009)
MR 121 SE (Roche Diagnostics)	532 nm	10 ps	793 nm	107 ps	10.4 mW	~ 50 nm (z)	M. Dyba et al., Nat. Biotech. 21, 1303 (2003)
Pyridine 2 / LDS 722 (Exciton, Radiant Dyes GmbH)	554 nm	250 fs	745 nm	50-200 ps	12.2 mW	44 nm (z)	M. Dyba et al., New. J. Phys. 7, 134 (2005)
RH 414 (Biotium, Inc.)	554 nm	250 fs	745 nm	13 ps	8.78 mW	30 nm (z)	M. Dyba, S.W. Hell, Phys. Rev. Lett. 88, 163901 (2002)
Pyridine 2 / LDS 722 (Exciton, Radiant Dyes GmbH)	554 nm	250 fs	760 nm	13 ps	-	33 nm (z)	M. Dyba, S.W. Hell, Phys. Rev. Lett. 88, 163901 (2002)
ATTO 590 (ATTO-TEC GmbH)	570 nm	~ 90 ps	690 nm	~ 90 ps	1.4-2.4 mW	30-40 nm (xy)	D. Wildanger et al., Opt. Expr. 16, 9614 (2008)
ATTO 590 (ATTO-TEC GmbH)	570 nm	~ 90 ps	690 nm	~ 90 ps	3.8 mW	20 nm (xy), 45 nm (xy), 108 nm (z)	D. Wildanger et al., J. Microsc. 236, 35 (2009)
ATTO 633 (ATTO-TEC GmbH)	630 nm	~ 90 ps	735 nm	~ 90 ps	1.4-2.4 mW	30-40 nm (xy)	D. Wildanger et al., Opt. Expr. 16, 9614 (2008)
ATTO 633 (ATTO-TEC GmbH)	635 nm	100 ps	750 nm	~ 200 ps	-	40 nm (xy)	A. Punge et al., Micr. Res. Techn. 71, 644 (2008)
ATTO 647N (ATTO-TEC GmbH)	635 nm	cw	750 nm	cw	423 mW	~ 50 nm (xy)	K. Willig et al., Nat. Meth. 4, 915 (2007)
ATTO 647N (ATTO-TEC GmbH)	635 nm	120 ps	750 nm	200 ps	-	< 40 nm (xy)	L. Meyer et al., Small 4, 1095 (2008)
JA 26 (K.H. Drexhage, Siegen University)	635 nm	68 ps	775 nm	300 ps	-	16 nm (x)	V. Westphal, S.W. Hell, Phys. Rev. Lett. 94, 143903 (2005)

ATTO 647N (ATTO-TEC GmbH)	635 nm	100 ps	780 nm	300 ps	-	~ 65 nm (xy)	G. Donnert et al., Biophys. J.: Biophys. Lett., L67 (2007) V. Westphal et al., Science 320, 247 (2008)
JA 26 (K.H. Drexhage, Siegen University)	635 nm	68 ps	780 nm	300 ps	90-100 mW	47 nm (xy)	V. Westphal et al., J. Phys. B: At. Mol. Opt. Phys. 38, S695 (2005)
JA 26 (K.H. Drexhage, Siegen University)	635 nm	68 ps	781 nm	303 ps	10.1 mW	40 nm (x)	V. Westphal et al., Appl. Phys. B. 77, 377 (2003)
JA 26 (K.H. Drexhage, Siegen University)	637 nm	54 ps	778 nm	303 ps	-	120-140 nm (xy)	V. Westphal et al., Appl. Phys. Lett. 82, 3125 (2003)
ATTO 565 (ATTO-TEC GmbH)	1060 nm	300 fs	676 nm	cw	200 mW	~ 70 nm (xy)	G. Moneron, S.W. Hell, Opt. Expr. 17, 14567 (2009)
KK114	630 nm		750 nm		2.3 mW	~ 80 nm (xy)	Wildanger, D., Buckers, J., Westphal, V., Hell, S., Kastrup, L., Opt. Expr. 17(18), 16100 (2009)
24 nm crimson beads (Invitrogen Corp.)	635 nm	70 ps	735 nm	300 ps	-	< 25 nm (xy)	Harke, B., Keller, J., Ullal. C., Westphal, V., Schonle, A., Hell, S., Opt. Expr. 16(6), 4154 (2008)
GFP	488 nm	-	560 nm	900 ps	4 mW	< 60 nm (xy)	Rankin, B. et al., Biophysical Journal, 100, L63 (2011)

This table has been adapted from the list of dyes used in STED microscopy given at <http://www3.mpibpc.mpg.de/groups/hell/>.